Part III: Polarization Modes

Chapter 6

Modeling of polarization mode competition in fiber DFB lasers[1]

Abstract — A comprehensive model for steady state analysis of polarization mode competition in fiber distributed feedback (DFB) lasers is presented. Effects of polarization dependent grating non-uniformities, polarization dependent grating strength, coupling between the linear polarization states due to twist or Faraday rotation, back reflections, cross-saturation from serially multiplexed lasers, as well as spatially and polarization dependent gain hole-burning are covered by the model. Regimes of single and dual polarization operation are identified for different types of polarization imperfections in the cavity. The output powers of the individual modes and the magnitudes of the hole-burning mechanisms are also calculated and discussed.

Index Terms — DFB lasers, fiber lasers, gain hole-burning, laser mode competition

6.1 Introduction

The fiber distributed feedback (DFB) laser was first demonstrated in 1994 [1]. Since then, promising results have been obtained in understanding and improving the processes governing output power efficiency and output intensity

[1]This chapter contains a re-edited version of [E. Rønnekleiv, M. N. Zervas and J. T. Kringlebotn, "Modelling of Polarization Mode Competition in Fiber DFB Lasers", IEEE J. of Quantum El., Vol. 34, pp. 1559-1568, 1998] which has been modified to include the corrections and the extensions to theory contained in [E. Rønnekleiv, M. N. Zervas and J. T. Kringlebotn, "Correction to "Modelling of Polarization Mode Competition in Fiber DFB Lasers"", IEEE J. of Quantum El., Vol. 35, pp. ??, July 1999].

noise from these devices [2], [3]. Advances in fiber Bragg grating technology also indicates that it soon will be possible to produce high quality fiber DFB lasers with high reproducibility and yield.

One motivation for investigating polarization mode competition (PMC) in fiber DFB lasers is the possibility of using dual polarization fiber DFB lasers as sensor elements in polarimetric sensor applications. By measuring the beat-frequency between the polarization modes, the birefringence within the laser cavity can be determined with high accuracy [4]. However, as observed in [4], maintaining robust dual polarization operation in sensor lasers may be difficult due to non-uniformity of the birefringence changes introduced when the laser is brought into contact with the measurand.

Another motivation for this work is the requirement of single polarization operation in lasers for telecommunication applications. Single polarization has been observed in experiments [2], [3], [5]-[7], but the qualitative and quantitative understanding of the requirements for single or dual polarization operation is still poor.

Since Kogelnik *et. al.* introduced the DFB laser and applied the coupled mode theory to model such a laser in [8], much work has been dedicated to the modeling and understanding of semiconductor DFB lasers [9]-[11]. Much of this work is also relevant for fiber DFB-lasers. However, there are also important differences between semiconductor and fiber lasers, regarding waveguide geometries, gain medium properties and the maximum available grating strength (κL). These differences call for a separate treatment of fiber lasers, like in [12]. PMC has not been much discussed in relation to semiconductor lasers, since robust single polarization operation seems easily obtainable in the non-circular waveguide geometries used.

PMC in fiber DFB lasers depends on a number of parameters and effects. These include non-uniform birefringence, twist of the birefringence axes, polarization dependence of the grating strength, back reflections, gain cross-saturation from other lasers in serially multiplexed systems, as well as gain hole-burning effects. The work presented in this paper is aimed at obtaining a better understanding of these effects and how they affect the laser operation.

The organization of this paper is as follows: In Section 6.2 we generalize the DFB coupled mode equations to include polarization coupling from twist or Faraday rotation. The grating super-mode solutions are introduced and briefly discussed. Section 6.3 introduces the gain saturation model used in our simulations, and Section 6.4 presents a way of quantifying the contributions to PMC from various gain hole-burning mechanisms. In Section 6.5, simulation results are presented that illustrate the effects of various types of polarization imperfections on the requirements for single or dual mode laser operation. Section 6.6 contains some concluding remarks. Details on the calculations of

the polarization gain hole-burning, spatial distributions of different gain hole-burning contributions, and a description of the numerical algorithm used for the simulations are given in Appendixes 6.A, 6.B, and 6.C respectively.

6.2 Coupled Mode Formulation

The electric field $\vec{E}\,(z,t)$ in a birefringent single mode fiber Bragg grating may be decomposed into the complex amplitudes of four intrinsic fiber modes. By "intrinsic" modes we mean the linearly polarized propagation modes when gain, loss and grating perturbations are removed. In vector notation we may write:

$$\vec{E}\,(z,t) = \mathbf{F}\,\vec{A}\,e^{i\omega t}\,; \quad \mathbf{F} = \begin{bmatrix} e^{-iK_B z} & 0 & 0 & 0 \\ 0 & e^{-iK_B z} & 0 & 0 \\ 0 & 0 & e^{iK_B z} & 0 \\ 0 & 0 & 0 & e^{iK_B z} \end{bmatrix}$$

with $\vec{A} = [\ r_x \quad r_y \quad s_x \quad s_y\ ]^T$. r and s represent the forward and backward propagating modal field amplitudes, respectively, and the subscripts x and y distinguish the polarization modes. Superscript T is used for matrix transposition. The phase of the elements of $\vec{A}$ are normalized with respect to the Bragg wave-number $K_B = \pi/\Lambda$, Λ being the grating period, through the diagonal matrix $\mathbf{F}$. ω, t and z denote frequency [rad/s], time and position along the fiber axis, respectively.

We assume K_B to be independent on z and express the propagation constants of the intrinsic polarization modes as

$$\beta_m = K_B + \Delta\beta_m + \delta\,; \quad m = x,\, y. \tag{6.1}$$

$\Delta\beta_m$ is the deviation due to birefringence and z-dependence of the refractive index. $\delta = (\omega - \omega_0)\,\partial\beta/\partial\omega$ (rad/m) is the detuning referenced to a nominal Bragg frequency $\omega_0 = K_B c/n$. c is the speed of light in vacuum and n is a nominal refractive index which is independent of polarization and position.

The polarization mode coupling originating from twist of the birefringence axes or Faraday rotation is deduced in [13] and [14]. A model for coupling between forward and backward propagating waves due to the index and gain gratings, including the effects of the mean gain or loss, is deduced in [11]. We here combine these effects in a 4-mode matrix coupling equation:

$$\frac{d\vec{A}}{dz} = \mathbf{C}_{tot}\vec{A}; \quad \mathbf{C}_{tot} = \mathbf{C} + \mathbf{G} + \mathbf{D}. \tag{6.2}$$

Here

$$\mathbf{D} = \begin{bmatrix} -1 & 0 & 0 & 0 \\ 0 & -1 & 0 & 0 \\ 0 & 0 & 1 & 0 \\ 0 & 0 & 0 & 1 \end{bmatrix} i\delta$$

$$\mathbf{G} = \begin{bmatrix} g & 0 & g_{gr} & 0 \\ 0 & g+\Delta g & 0 & g_{gr}+\Delta g_{gr} \\ -g_{gr}^* & 0 & -g & 0 \\ 0 & -g_{gr}^*-\Delta g_{gr}^* & 0 & -g-\Delta g \end{bmatrix}$$

$$\mathbf{C} = \begin{bmatrix} -d_x & r+\rho & i\kappa_x & 0 \\ -r-\rho & -d_y & 0 & i\kappa_y \\ -i\kappa_x^* & 0 & d_x & r-\rho \\ 0 & -i\kappa_y^* & -r+\rho & d_y \end{bmatrix}$$

and

$$d_m = i\Delta\beta_m - a\,.$$

For practical reasons we have divided the total coupling matrix $\mathbf{C}_{tot}$ into three parts. $\mathbf{D}$ contains the frequency dependence. $\mathbf{G}$ contains parameters that are dependent on the pumping and saturating fields, and $\mathbf{C}$ contains the remaining signal- and frequency-independent parameters.

g is the amplitude gain coefficient (resulting from the gain medium) and g_{gr} is the (complex) gain grating amplitude. Δg and Δg_{gr} are the gain and gain grating differences between the birefringence axes due to polarization hole-burning (PHB). a is the intrinsic loss coefficient and κ_m is the index coupling strength in the $m = x$ or y mode. The complex conjugation of κ_m in the lower left part of $\mathbf{C}$ is included for completeness only, since the assumption of a z-independent Bragg period means that κ_m can always be assumed to be real. The polarization coupling parameters r and ρ (rad/m) represent the twist rate of the birefringence axes and the Faraday rotation coefficient (in case of magnetic fields present), respectively. Note that in the case of twist, the field vector components of $\vec{A}$ refer to a twisted coordinate system that follows the birefringence axes of the fiber.

The general solution of (6.2) may be written as a linear combination of four grating "super-modes":

$$\vec{A} = \sum_{i=1}^{4} a_i\,\vec{u}_i e^{-(\gamma_i + i\zeta_i)z} \tag{6.3}$$

The eigenvectors $\vec{u}_i$ and propagation constants $-(\gamma_i + i\zeta_i)$ are the eigenvectors and eigenvalues of $\mathbf{C}_{tot}$. ζ_i may be interpreted as the difference between the

spatial frequency of the super-mode and the Bragg wave-number K_B. γ_i is the modal attenuation coefficient. In general the eigenvalues occur in reciprocal pairs with opposite signs of ζ_i and γ_i.

With no cross-coupling between the polarization states (r, $\rho = 0$) the linear polarizations are decoupled, leading to two x- and two y-polarized super-modes. The full dispersion map of one such mode, in absence of any gain, loss or gain grating, was illustrated in [15]. Within the stop-band of each polarization, given by $|\delta + \Delta\beta_m| < \kappa_m$, there is a reciprocal set of two super-modes with $\zeta_i = 0$ and $\gamma_i = \pm\sqrt{(\delta + \Delta\beta_m)^2 + \kappa_m^2}$.

With the gain or loss magnitudes usually present in fiber DFB lasers (g, g_{gr}, $a \ll \kappa_m$), the modifications of the eigen-solutions in (6.3) are small. In an ideal half-period phase-shifted DFB laser operating in the fundamental longitudinal laser mode, the super-modes with $\gamma_i < 0$ will dominate to the left of the grating phase-shift and those with $\gamma_i > 0$ will dominate to the right. Since the laser operates at the center of the stop-band, the intensity will decay with an exponential rate of $2\gamma_{max} = \pm 2\kappa_m$ from the phase-shift position, where γ_{max} is the value of γ_i at the center of the stop band. This κ_m-dependence of the decay rate is important for the interpretation of simulation results in section 6.5

6.3 Gain Model

We have focused on Er-doped amplifier media, which can be modelled by the 2-level rate equations [16]. At a position z in the cavity the local amplitude gain is approximated as:

$$g_{loc}(\phi) = \frac{g_{unsat}}{1 + P_s/P_{sat}}; \quad g_{unsat} = \frac{a_p r_{wl} P_p}{P_{sat}} - a_s \tag{6.4}$$

with

$$\begin{aligned} P_{sat} &= \left([g_p + a_p]\, r_{wl} P_p + P_{sp}/2\right)(g_s + a_s)^{-1} \\ P_s &= \sum_{m=1}^{N_m} \left(\left|\vec{R}_m\right|^2 + \left|\vec{S}_m\right|^2 + 2\,\mathrm{Re}\left(e^{i\phi}\vec{S}_m^{+}\vec{R}_m\right)\right). \end{aligned}$$

Here $\phi = 2K_B z$ describes the phase relative to the index grating. g_{unsat} is the unsaturated gain, P_{sat} is the saturation power at the signal wavelength, and P_p and P_s are the pump and signal powers. $\vec{R}_m = [r_x,\, r_y]_m$ and $\vec{S}_m = [s_x,\, s_y]_m$ are the right and left propagating fields of laser mode m, $m = 1..N_m$. This notation covers any number N_m of lasing modes. In the following sections, when only two polarization modes are involved, the letters $m = x, y$ will be used as mode indexes. $\vec{S}_m^{+}$ is the transposed conjugate of $\vec{S}_m$. The gain medium parameters

g_s, g_p, a_s and a_p represent signal and pump gain at full inversion and signal and pump absorption at zero inversion, respectively. $P_{sp} = n_{Er} h\nu_s / \tau_{sp}$ (W/m) is the spontaneous emission power per unit length of fiber at full inversion, with τ_{sp} being the spontaneous emission time, $h\nu_s$ the signal photon energy, and n_{Er} the ion concentration per unit fiber length. r_{wl} is the ratio of the pump wavelength to the signal wavelength.

The gain and gain grating coefficients g and g_{gr} that appear in (6.2) are given by the zeroth and first order Fourier components of $g_{loc}(\phi)$, respectively [17], [18]. Based on (6.4) we generalize the expressions in [17] and [18] to allow for multiple and arbitrarily polarized laser modes:

$$\begin{aligned} g &= g_{unsat} \left[(1 + p_{tot})^2 - 4 |p_c|^2 \right]^{-1/2} \\ g_{gr} &= \frac{g_{unsat}}{2 p_c^*} \left[1 - (1 + p_{tot}) \left[(1 + p_{tot})^2 - 4 |p_c|^2 \right]^{-1/2} \right] . \end{aligned} \tag{6.5}$$

Here

$$p_{tot} = \sum_{m=1}^{N_m} \frac{\left|\vec{R}_m\right|^2 + \left|\vec{S}_m\right|^2}{P_{sat}}; \quad p_c = \sum_{m=1}^{N_m} \frac{\vec{S}_m^{+} \vec{R}_m}{P_{sat}}.$$

Note that the gain grating coefficient g_{gr} has the same phase as the normalized standing wave power phasor p_c.

The pump absorption follows from the rate equations as:

$$a_{pump} = a_p - \frac{g_p + a_p}{g_s + a_s} (g + a_s) . \tag{6.6}$$

Eqs. (6.4) to (6.6) cover the spatial hole-burning mechanisms. In addition, polarization hole-burning (PHB) should be included in the model. PHB effects in erbium-doped fiber amplifiers (EDFAs) have been studied in [19]-[22], and comprehensive ion anisotropy models as well as simplified approximate formulas are presented in [21] and [22]. However, those simplified formulas do not describe a reduction of the PHB magnitude at high gain compressions ($P_s / P_{sat} > 1$) predicted by the comprehensive models. Numerical implementation of the comprehensive ion anisotropy models (c.f. Appendix 6.A) indicates that the local gain difference between the polarization state of the saturating signal and the orthogonal state Δg_{loc} may be approximated by:

$$\frac{\Delta g_{loc}}{g_{unsat}} \approx \frac{\eta \, D_p \, P_s / P_{sat}}{(1 + P_s / P_{sat})^2}. \tag{6.7}$$

Here D_p is the degree of linear polarization of the total power at the lasing wavelength, defined in our model by (6.8) below. η is a material parameter

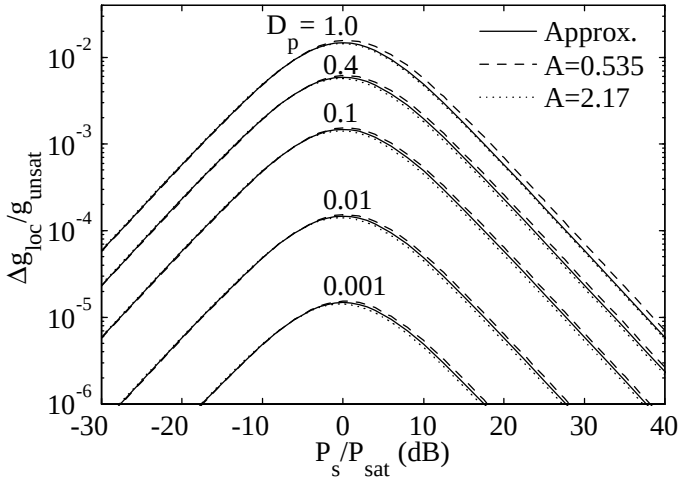

Figure 6.1. Normalized local PHB magnitude $\Delta g_{loc}/g_{unsat}$ versus normalized saturating power P_s/P_{sat} with various degree of linear polarization D_p. Solid lines: Approximation (6.7) with $\eta = 0.059$. Dashed/dotted lines: Model of Wysocki et. al. [15].

that depends on the magnitude of the ion anisotropy. When estimating η from PHB measurements on EDFAs, it is necessary to eliminate the effects of the random evolution of D_p along the EDFA, as well as the contribution to the measured EDFA saturation from pump absorption. Wysocki *et.al.* [21] have taken these effects have been taken into account when estimating the ion anisotropy parameter (ratio of ion cross-sections orthogonal and parallel to the optical axis of each ion, c.f. Appendix 6.A.) for an EDFA fiber to $A = 0.535$ or $A = 2.17$. Based on those estimates we estimate $\eta = 0.059$ in Appendix 6.A.

Fig. 6.1 illustrates the dependence of $\Delta g_{loc}/g_{unsat}$ on P_s/P_{sat} and D_p approximated by (6.7) with $\eta = 0.059$ (solid lines), and calculated from Wysocki's model [21] (dashed and dotted lines). The approximation error is within $+10\%$ and -18%. Note the drop in Δg_{loc} at high intensities. (6.7) may be reduced to $\Delta g_{loc} \approx \eta D_p(g_{unsat} - g_{loc})$ for $P_s \ll P_{sat}$, where g_{loc} is the saturated gain. This is consistent with previously published approximations.

In a dual polarization laser the saturating power will be only partly polarized, since the combined polarization state within the cavity oscillates at the beat frequency between the laser modes. The degree of polarization may vary spatially over a standing wave period if the standing waves in the two polarizations are not in phase. However, in those cases the spatial hole-burning effect on the PMC due to g_{gr} is expected to dominate over the PHB effects due to the polarization dependence Δg_{gr} of g_{gr}, and no significant error in the simulations should thus be introduced by ignoring this spatial modulation of D_p. For use in

our model we therefore define an effective degree of polarization as the signed quantity in terms of the mean x- and y-polarized signal powers averaged over one standing wave period, denoted P_x and P_y:

$$\begin{aligned} D_p &\approx (P_x - P_y) / (P_x + P_y) \\ &= \frac{1}{p_{tot} P_{sat}} \sum_{m=1}^{N_m} \left(|r_{x,m}|^2 + |s_{x,m}|^2 - |r_{y,m}|^2 - |s_{y,m}|^2 \right). \end{aligned} \tag{6.8}$$

As explained in Appendix 6.A, (6.7) leads to the following expressions for the polarization dependent gain parameters of (6.2) provided that D_p is does not vary over the standing wave period:

$$\begin{aligned} \Delta g &= \eta D_p \frac{\left(p_{tot} + p_{tot}^2 - 4 |p_c|^2\right)}{\left[(1+p_{tot})^2 - 4 |p_c|^2\right]^{3/2}} \\ \Delta g_{gr} &= \frac{\eta D_p}{2 p_c^*} \left\{ 1 + \frac{\left(8 |p_c|^2 + 4 |p_c|^2 p_{tot} - (1+p_{tot})^3\right)}{\left[(1+p_{tot})^2 - 4 |p_c|^2\right]^{3/2}} \right\}. \end{aligned} \tag{6.9}$$

It may be noted that PHB contributions due to the circularly polarized part of the saturating field, reported in [20], are not taken into account in (6.9). However, for the present simulations (Section 6.5) the field ellipticities are low or zero, and the omission of this effect should not affect the results significantly.

6.4 Quantitative measures of gain saturation

In earlier work [8]-[11] the single-pass gain parameter, defined as the gain experienced by a probe beam passing through the laser without interacting with the reflectors, was used to study and compare modal thresholds. This parameter, however, cannot reveal the important effect of gain hole-burning on multi-moded laser operation.

An alternative measure for the threshold gain requirements of mode m is the contribution rtg_m from the gain medium to the total modal round-trip gain RTG_m (defined in Appendix 6.B). This parameter may be defined as:

$$rtg_m = \frac{P_{gain}}{P_c} \tag{6.10}$$

where P_{gain} is the power transferred from the gain medium to the laser mode and $P_c = \left|\vec{R}(z_c)\right| \cdot \left|\vec{S}(z_c)\right|$ is the geometric mean of the modal powers travelling in the right and left direction at the center z_c of the laser. rtg_m compensates exactly the cavity losses of any lasing mode.

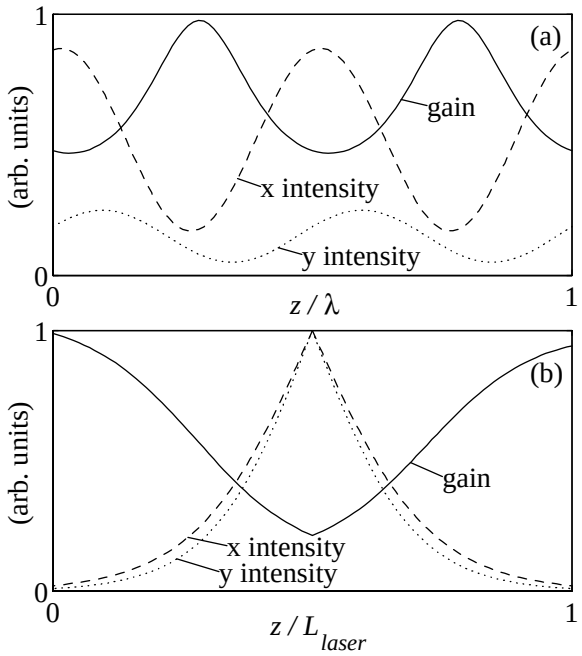

Figure 6.2. Examples of (a) local spatial hole-burning (LSHB) and (b) global spatial hole-burning (GSHB).

The difference $\Delta rtg_{total} = rtg_y - rtg_x$ between the gain contributed to the laser polarization modes ($m = x, y$) must be due to the spatial and polarization hole-burning mechanisms, i.e. different effective overlaps in space and polarization between the gain distribution and the modal intensity distributions. Three contributing hole-burning mechanisms have been identified:

Δrtg_p PHB contribution due to the polarization dependence of g and g_{gr} (c.f. (6.9)).

Δrtg_l Local spatial hole-burning (LSHB) contribution which is present if the two modal standing wave patterns have different phases relative to the gain grating. This situation is illustrated in Fig. 6.2 (a).

$\Delta rtg_g = \Delta rtg_{total} - \Delta rtg_p - \Delta rtg_l$. Global spatial hole-burning (GSHB) contribution, which is due to the different global overlaps of the modal field distributions and the gain, as illustrated in Fig 6.2 (b).

A more detailed description of how the hole-burning contributions are calculated is given in Appendix 6.B.

6.5 Simulation Results

A numerical approach, described in Appendix 6.C, has been used to compute the expected PMC behavior of fiber DFB lasers with different types of polarization imperfections. By polarization imperfections we mean asymmetries between polarization states that cause differences between the output powers of the two polarization modes. The expressions for mode-coupling, gain saturation and pump absorption described in Sections 6.2 and 6.3 were used for the calculations.

The basic structure to which the polarization imperfections were added was a $L = 70$ mm uniform grating with a π (half period) phase-shift in the center. The gain medium parameters used were $[g_s, g_p, a_s, a_p] = [22, 2.74, 20, 8]$ dB/m, $P_{sp} = 5.2$ mW/m, $r_{wl} = 0.961$, and $\eta = 0.059$. These numbers are representative for a highly Er-doped fiber pumped at 1480nm and lasing at 1540nm, with a maximum gain (when $P_p \to \infty$) at the laser wavelength of 11.3 dB/m, and with a pump saturation power of 2.95 mW. The intrinsic loss a was assumed to be zero. A pump power of $P_{p0} = 50$ mW launched from the left end ($z = 0$) was assumed for all the simulations.

Note that due to the scaling properties of the coupling equation (6.2), all results given in this section are valid for any scaling of the z-axis, provided that the normalized values for the detuning $\delta_m L$, gain medium parameters $g_s L, g_p L, a_s L, a_p L$ and the parameters contained in $\mathbf{C}L$ are all preserved.

The main results are plotted in Figs. 6.3-6.5, 6.7, 6.8, and 6.11, with the magnitudes of different polarization imperfections along the respective horizontal figure axes. Row (a) of these figures shows the regimes of grating strength κL that cause single and dual polarization operation. The single and dual mode thresholds computed were, except for the case with cross-saturation in Fig. 6.10, found to be quite insensitive to further increases of the pump power towards infinity.

In row (b) the magnitudes of the different gain hole-burning contributions at the border between the single and dual polarization regimes of row (a) are illustrated with curves for Δrtg_l, $\Delta rtg_l + \Delta rtg_p$ and Δrtg_{total}, c.f. Section 6.4. Note that Δrtg_g is given implicitly by the relation $\Delta rtg_{total} = \Delta rtg_l + \Delta rtg_p + \Delta rtg_g$.

In row (c) $\kappa L = 9$ is assumed. The absorbed pump power and the total output power (right+left) of both laser modes are plotted. The left to right output power ratio of the individual modes (not displayed) was found to be within 1 ± 0.002 in all cases, except for the case of back reflection in Fig. 6.9. In that case the left to right output ratios was within 1 ± 0.05 for back reflections below -32 dB.

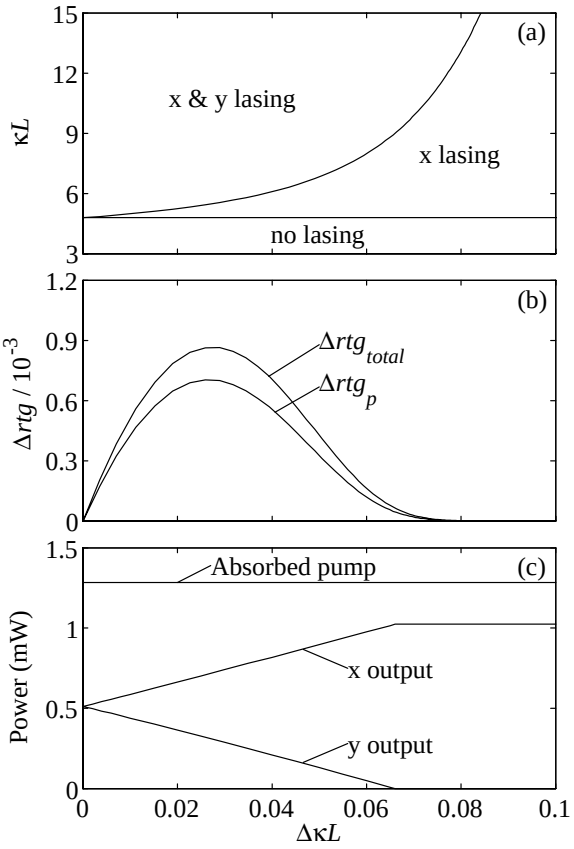

Figure 6.3. (a) Regimes of single and dual polarization operation, (b) differential gain contributions ($\Delta rtg_l = 0$ in this case) and (c) output power and absorbed pump power. All quantities are plotted against a polarization dependence of the grating strength $\Delta\kappa L$.

6.5.1 Polarization dependent grating strength

Fig. 6.3 illustrates how the PMC evolves with a polarization dependence of the grating strength, quantified by $\Delta\kappa L$ where $\kappa = \kappa_x$ and $\Delta\kappa = \kappa_x - \kappa_y$.

Fig. 6.3 (a) shows that the dual polarization threshold increases slowly at low polarization imperfection magnitudes. At higher magnitudes, $\Delta\kappa L \gtrsim 0.04$, the slope of the threshold starts increasing progressively. The single polarization threshold stays unchanged, as expected since the grating strength κ_x experienced by the first lasing mode is not changed.

From Fig. 6.3 (b) we see that the hole-burning contribution Δrtg_{total} to the differential round-trip gain at the dual polarization threshold increases towards a maximum at $\Delta\kappa L = 0.027$ and then decreases for higher imperfection magnitudes, approaching zero very rapidly for $\Delta\kappa L \gtrsim 0.06$. Δrtg_{total} is seen to be composed mainly from the PHB contribution Δrtg_p at low values of

$\Delta\kappa L$. The LSHB contribution is zero, since the phase of the modal standing wave intensity modulation is independent on the coupling parameter $\kappa_{x,y}$. The GSHB contribution $\Delta rtg_g = \Delta rtg_{total} - \Delta rtg_p$ contributes somewhat, due to the different spatial decay rates of modal intensities from the center of the cavity (c.f. the end of section 6.2).

The cold cavity round-trip loss rtg_{loss} for a mode may be expressed as the ratio between the total laser output power arising from that mode and the modal power travelling in one direction at the center of the grating. It can be shown (c.f. the end of Sec. 6.2) that

$$rtg_{loss} \approx 8\exp(-\kappa L)) \tag{6.11}$$

The difference in rtg_{loss} between the polarization modes due to $\Delta\kappa$ must equal Δrtg_{total}, which implies the following relation:

$$\Delta rtg_{total} \approx 8\Delta\kappa L\exp(-\kappa L). \tag{6.12}$$

Analysis of the dual polarization thresholds and total hole-burning magnitudes plotted in Figs. 6.3 (a) and (b) confirm the relation (6.12).

The evolution of the dual polarization threshold κL versus $\Delta\kappa L$ in Fig.6.3 (a) is decided by the condition that the gain difference due to the hole-burning must match the gain difference in (6.12). The available hole-burning contribution depends on the effective level of the saturating signal intensity P_s within the cavity. As mentioned in Sec. 6.2, P_s decays exponentially on a global scale from the central phase-shift position, with an exponential decay rate of $2\kappa_{x,y}$. This decay implies that most of the stored laser energy is concentrated near the center of the grating. It follows from (6.11) that the saturating power P_s at the central phase-shift position equals $4\exp(\kappa L)$ times the one way laser output power. P_s in the central region of the cavity thus increases exponentially with κL.

At small values of $\Delta\kappa L$ we see from Fig.6.3 (a) that the dual polarization threshold value for κL is close to the single polarization threshold. The effective saturation intensity in the cavity therefore increases relatively slowly in this regime, due mainly to the increase in laser output power as κL increases above the single polarization threshold. The increase in Δrtg_p with $\Delta\kappa L$ within this regime may be explained by the increase in PHB magnitude with increasing saturating power for $P_s/P_{sat} < 1$, as seen in Fig. 6.1.

The laser output power saturates when κL increases well above the single mode threshold. The effective saturating power in the cavity is then essentially proportional to $4\exp(\kappa L)$. Fig. 6.1 and (6.7) show that the PHB is inversely proportional to P_s/P_{sat} at high saturating powers, and Δrtg_p is therefore essentially proportional to $\exp(-\kappa L)$ at these high κL-values. By comparing with

(6.12) we see that the increase in the required Δrtg_{total} as $\Delta\kappa L$ increases can not be compensated solely by the PHB in this regime by increasing κL. Actually, the ratio $\Delta rtg_g/\Delta rtg_p$ increases with $\Delta\kappa L$ in Fig. 6.3 (b), confirming that the GSHB plays an increasingly important role as $\Delta\kappa L$ increases.

Analytic approximations like the one in (6.12) for the required hole-burning at dual polarization operation are not available for the other types of polarization imperfections discussed in the following sub-sections. However, as seen from (6.11), the round-trip loss of each laser mode in an ideal cavity decreases exponentially with increasing κL. It is therefore reasonable to believe that differential losses introduced by other types of polarization imperfections will also decrease rapidly with increasing κL.

Fig. 6.3 (c) shows that for $\kappa L = 9$ the laser will be single-moded, as required for a telecommunication CW-source, when $\Delta\kappa L > 0.066$. For birefringence sensors applications a polarization output power ratio smaller than 2 is a reasonable requirement, for which $\Delta\kappa L < 0.023$ is needed.

Polarization dependencies up to 8 % of the total photoinduced index change was reported in [23], depending on the polarization of the UV-exposure and on fiber properties. One may expect similar values for $\Delta\kappa/\kappa$ in a photoinduced grating. Even higher values for $\Delta\kappa/\kappa$ were reported in [24] for a fiber with high stress-induced birefringence. Control of the polarization of the UV-exposure thus seems to be important for controlling the PMC in fiber DFB lasers.

6.5.2 Polarization dependent chirp

Fig. 6.4 illustrates how PMC depends on chirp of the y polarization propagation constant β_y. This is equivalent to chirping of the y polarization Bragg wavelength while the x polarization Bragg wavelength is kept constant. Solid and dashed lines illustrate linear and square chirp, respectively, as given by (c.f. (6.1))

$$\begin{array}{ll} \Delta\beta_y = \Delta\beta\,(z - L/2)/L & \text{(linear chirp)} \\ \Delta\beta_y = 4\,\Delta\beta\,(z - L/2)^2/L^2 & \text{(square chirp).} \end{array} \tag{6.13}$$

The results in Fig. 6.4 are qualitatively similar to those shown for the polarization dependent grating strength in the previous section, except for he dual polarization threshold for the square chirped laser in Fig. 6.4 (a) which shows signs of saturating for $\Delta\beta L \gtrsim 5$. Unlike the case illustrated in the last section, there are also some contributions to Δrtg_{total} from LSHB in the chirped lasers, since the standing wave phase is affected by the polarization dependent variations of the propagation constant throughout the cavity.

Polarization dependent chirp may be due to any source of birefringence that is non-uniformly distributed along the fiber, such as UV-exposure (c.f. previous section), externally applied transverse forces, bending, internal stress in

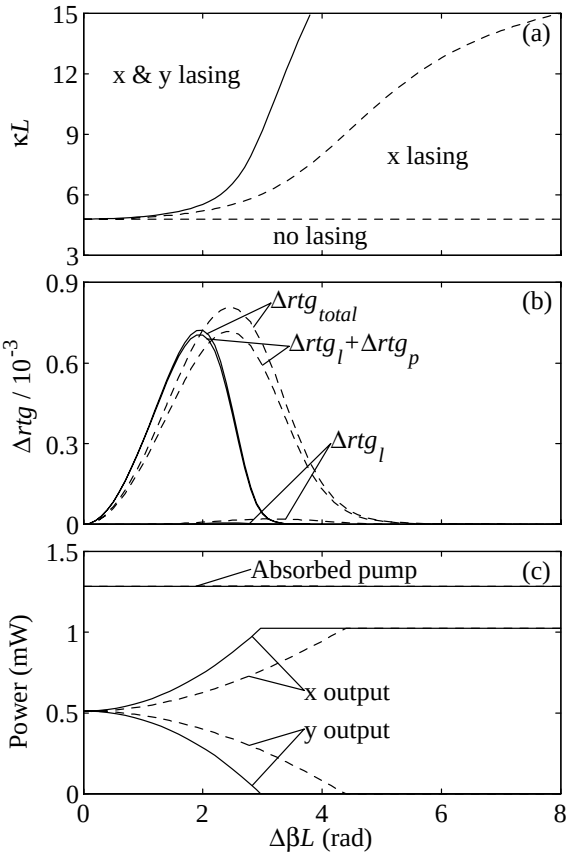

Figure 6.4. Same information as in Figure 6.3 plotted against linear chirp (dashed lines) and square chirp (solid lines) of β_y, c.f. eq. (6.13).

the fiber, or core ellipticity. In some sensor applications, where external forces are supposed to act on the fiber, the uniformity of some of these effects may be difficult to control. On the other hand, single polarization operation for telecommunication lasers may be achieved by manipulating the birefringence intentionally.

The assumption of chirp in only one axis, which has been used here, may not be realistic in many cases. Theoretical calculations of stress-induced birefringence suggest a ratio $\Delta\beta_y/\Delta\beta_x = -2.5$ for bending [14] and $\Delta\beta_y/\Delta\beta_x \sim -5$ for transverse forces applied externally to the fiber [14], [25], [26]. In the case of transverse forces, however, these calculations do not take common mode index change due to axial stress or coating effects into account, and experimental results have been published with differing $\Delta\beta_y/\Delta\beta_x$ ratios. In [4] a ratio of 50 was observed with an uncoated fiber DFB laser. Measurements on passive Bragg gratings show ratios of 7 for an uncoated fiber [27] and 1.37 for an acrylate coated fiber [28]. In the acrylate-coated case a significant chirp would

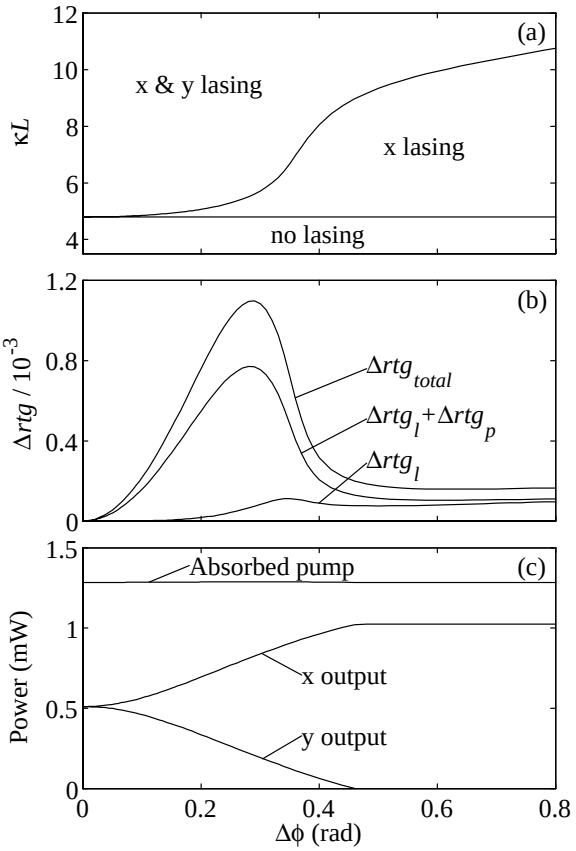

Figure 6.5. Same information as in Figure 6.3 plotted against a grating phase error $\Delta\phi$ in the y polarized mode localized to the center of the grating.

thus be imposed in both polarizations, and the curves in Fig. 6.4 would not be quantitatively representative.

According to the theory $\Delta\beta_y L = 1$ corresponds to a bending diameter of about 20mm or to axial forces in the order of 0.04N/mm in a fiber DFB laser of length $L = 70$ mm.

6.5.3 Polarization dependent phase error

Fig. 6.5 illustrates how PMC depends on a grating phase error (round-trip phase) $\Delta\phi$ in the y propagation mode only, localized at the center of the grating.

For comparison, the square chirp (dashed lines) in Fig. 6.4 can be viewed as a highly distributed phase error of magnitude $\Delta\phi \sim \Delta\beta L$. By comparing Figs. 6.4 (a) and 6.5 (a) we see that the dual mode threshold is much more sensitive to localized phase errors. The spatial hole-burning effects, though, are seen to be stronger in Fig. 6.5 (b) than in Fig. 6.4 (b).

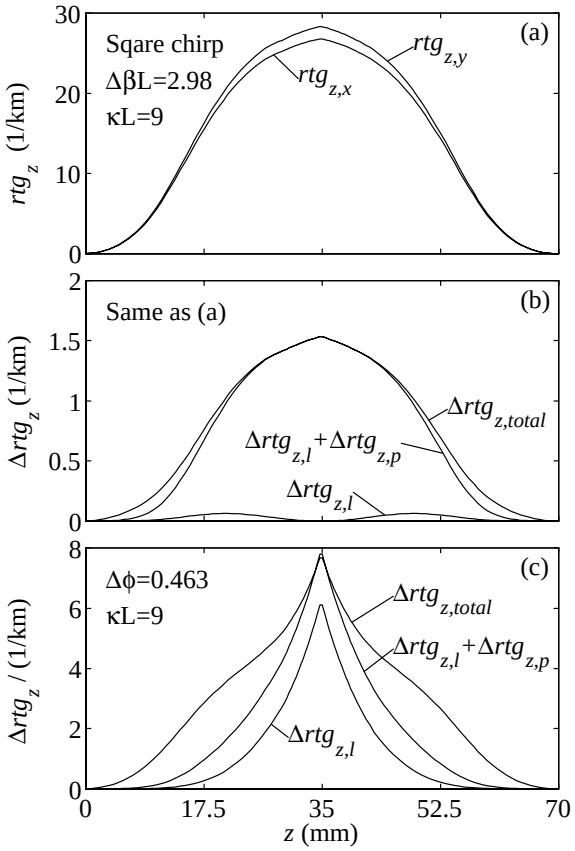

Figure 6.6. Spatial gain and differential gain contributions at the dual polarization threshold when $\kappa L = 9$. (a) Modal round-trip gain contributions for the square chirped laser illustrated with dashed lines in Fig. 6.4 (b). (b) Differential gain contributions for the same laser as in (a). (c) Differential gain contributions for the laser illustrated in Fig. 6.5 (b).

To give an indication of how the gain contribution per unit length to the individual modes may look like, the z-derivatives $rtg_{z,x}$ and $rtg_{z,y}$ of the modal gain contributions (i.e. the integrand of (6.15)) are plotted in Fig. 6.6 (a) for the square chirp case of (6.13) with $\Delta\beta L = 2.98$ and $\kappa L = 9.0$, i.e. at the dual polarization threshold of Fig. 6.5 (c). The relatively flat shapes of $rtg_{z,x}$ and $rtg_{z,y}$ indicate a strong saturation of the gain near the center, since the power penetration depth is only $(2\kappa)^{-1} = 3.9$ mm.

The z-distributions of the hole-burning contributions are illustrated in Fig. 6.6 (b) for the same laser as the one illustrated in Fig. 6.6 (a). Fig. 6.6 (c) shows the z-distributions of the different hole-burning contributions at the dual polarization threshold for a laser with a localized phase error, with $\kappa L = 9.0$ and $\Delta\phi = 0.463$. The relatively strong spatial hole-burning effect near the

phase-shift position in Fig. 6.6 (c) may be explained by considering the phase of the standing wave pattern of the y-mode relative to the index grating, which close to the phase-shift position differs by $\pm\Delta\phi/2 = \pm 0.2315$ rad from its ideal value. This causes significant LSHB contributions in the central region, and it also increases the effective power penetration depth of the y-mode, giving rise to significant GSHB contributions further away from the center, as is clearly seen in the figure.

In Fig. 6.6 (b) the LSHB and GSHB contributions are close to zero. This reflects that the phase difference between the standing waves of the two modes stays small throughout the central part of the grating, implying similar global intensity decay rates for the two modes in this region. The deviation in the of the y-index grating phase from an ideal non-chirped grating occurs mostly near the ends of the cavity, and the differential cavity loss is therefore mainly due to different intensity decay rates for the two modes in these end regions.

Polarization dependent phase-shifts can be achieved by post-exposure of a few millimeters of the fiber after grating inscription, and stable single polarization lasers have been reported by use of this technique [7]. If the length of the exposed section is comparable to or longer than the power penetration depth $(2\kappa)^{-1}$, effects of the spatial distribution of the phase error is believed play a significant role.

6.5.4 Combination of twist and polarization independent phase error

Fig. 6.7 illustrates how PMC depends on a uniform twist of the fiber birefringence axes by r (rad/m), combined with a polarization independent phase error of 0.2 rad located at the center of the grating. The solid and dashed lines illustrate cases where the normalized intrinsic birefringence $(\Delta\beta_y - \Delta\beta_x)L = 0.44$ and 4.4, respectively, corresponding to beat-lengths of 1m and 0.1m. "x" and "y" labelling of the polarization modes refers to the directions of the major axes of the modal fields at the center of the grating.

Without the phase error, the laser modes would have equal thresholds and output powers. With the error present, the dual mode threshold is seen to increase towards infinity when moderate twist is applied. Above $rL \sim 5$ the threshold decreases towards a minimum at $rL \sim 9$, while the gain difference contributions from LSHB and GSHB increase. The threshold variations are generally larger for the high birefringence case (dashed lines).

The results in Fig. 6.7 indicate that single polarization operation can be achieved by writing a uniform birefringent DFB laser with an intentional phase error, and then twisting the grating. This has earlier been demonstrated experimentally in [29]. There are, however, differences between the laser behavior reported in [29] and our simulation results. In the experiment no change in the output power was observed until an offset twist rate of $rL \approx 1$ was reached. No

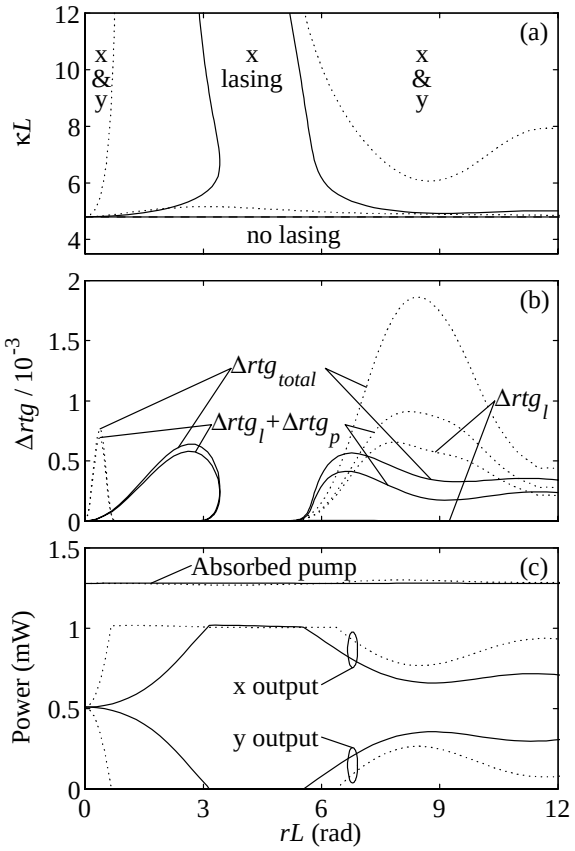

Figure 6.7. Same information as in Figure 6.3 plotted against twist rL assuming a polarization independent phase error of 0.2 rad at the center and intrinsic beat-lengths of 1m (solid lines) and 0.1m (dashed lines).

such effect is predicted from our simulations. Other differences in the shape of the output power versus twist rate may be related to different distributions of the grating phase errors in the experiment and the simulations. The changes in the beat frequency between the polarization modes observed in [29] are qualitatively similar to what we observed in the present simulations.

Fig. 6.8 shows (a) the z-dependence of the hole-burning effects, (b) the major axis orientations (MAO) of the forward and backward propagating modal fields $\vec{R}_m$ and $\vec{S}_m$, $m = x, y$ and (c) the ellipticity of the fields. The same parameters are assumed as for the laser illustrated with dashed lines in figure 6.7 (b), with $rL = 8.5$ and $\kappa L = 6.1$.

The plotted ellipticities are defined as the ratio of the minor to major axes, with positive sign for right hand rotation. The ellipticities are seen to be small (within ± 0.11) throughout the grating. At the outputs the ellipticities are still

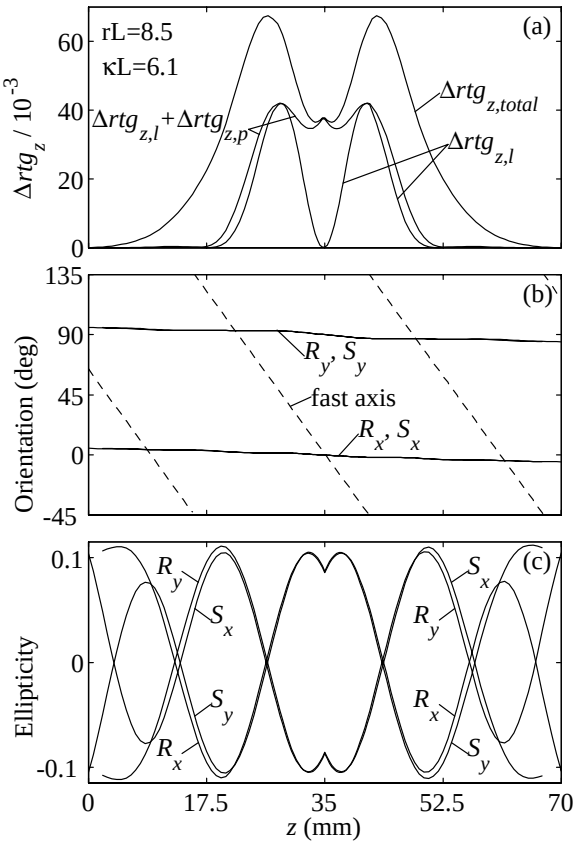

Figure 6.8. Spatial dependence of (a) differential gain contributions, (b) orientation of the major axes of $\vec{R}_m$ and $\vec{S}_m$, $m = x, y$, and (c) the ellipticity of $\vec{R}_m$ and $\vec{S}_m$ with $rL = 8.5$ for the laser illustrated with dashed lines in Figure 6.9 (b).

nonzero, though. This is in contrast to the findings for uniformly twisted Fabry-Perot lasers [30].

The MAO's are referenced to a non-twisted coordinate system. The orientation of the fast birefringence axis is included as a dashed line for reference. The MAO's are fairly constant throughout the grating. This means that throughout the grating each laser mode changes between propagating in the fast and slow intrinsic polarization modes. Consequently, the modal fields experience effectively positive and negative square chirps near the center of the grating. These effective chirp imperfections subtract and add to the polarization independent phase error of x- and y-modes, respectively, and thus explain why the polarization independent phase error changes the PMC behavior of the twisted DFB laser.

The rotation of the fast and the slow birefringence axes along the grating also "pulls" the two standing wave patterns out of phase with each other in certain

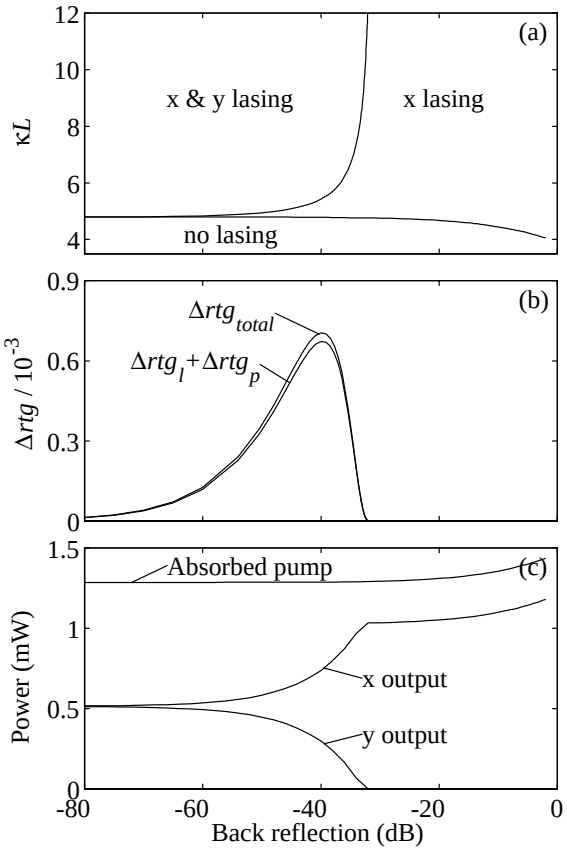

Figure 6.9. Same parameters as in Figure 6.3 plotted against back reflection level.

regions. This explains the high LSHB contribution in the regions around $z = 24$ mm and $z = 46$ mm.

Because of the stress-induced optical activity in silica fiber when it is twisted [14] the actual twist rate of the fiber will be $r_{act} \simeq 1.18r$, where r is the effective polarization coupling rate used in the simulations. Thus, the reference coordinates for Fig. 6.8 (b) will actually be twisted by $-0.18rL$ in a real silica fiber.

6.5.5 Back reflection

Fig. 6.9 shows how the PMC depends on back reflection into the right hand side ($z = 70$ mm) of the grating. The x and y output fields are assumed to be reflected with their polarization states maintained, while the phase-shift of the reflection differs by π between the two polarizations. The common reflection phase is selected such that the polarization output power ratio is maximized. It is believed that this combination of back reflection phases and polarization

states represents a worst case with respect to the polarization output power ratio.

The dual mode threshold in Fig. 6.9 (a) increases only slightly up to a back reflection level of −40 dB. Above this level the dual polarization threshold increases very rapidly, and with the given worst case back reflection phases, dual polarization operation cannot be achieved only by increasing κL when the back reflections are stronger than −30 dB. The output powers shown in Fig. 6.9 (c) are sums of the modal output powers to the left and the output at the right-hand side of the added reflector. One see that for the illustrated case of $\kappa L = 9$, the polarization output power ratio is >1.09 for back reflections above −60 dB. In real systems, where the back reflection phases and polarizations may change due to vibrations and temperature variations, this would imply worst case ripples in the polarization output power ratio of more than ±9 %. Typical back reflection levels obtainable when an isolator is placed between the laser output and connectors/detectors may be from −60 to −70 dB.

As seen from Fig. 6.9 (a), single mode operation can in principle be achieved for any κL in a birefringent fiber by introducing a bare fiber end back reflection (-15 dB) positioned 1/4 beat-length from the grating, ensuring a back reflection phase difference of π between the polarization modes. Some kind of tuning would be required, however, to assure the correct common mode phase-shift between the reflector and the grating.

Fig. 6.9 (b) shows that PHB is the dominating hole-burning effect in this case, with a small negative contribution from GSHB.

6.5.6 Serial multiplexing, cross-saturation by passing power

Fig. 6.10 shows the PMC behavior when optical power at a wavelength close to the laser wavelength (but not resonating with the grating) is passing through the laser in the y polarization state. This corresponds to a situation where several dual polarization lasers are multiplexed along the fiber, for instance as birefringence sensor elements. In most such situations the passing power will, however, be somehow divided between the polarization states, so the simulations represent a worst case.

As indicated earlier, the modal power near the center of the laser, where most of the round-trip gain contribution originates, will typically exceed the output power by several orders of magnitude. From this argument, the DFB laser operation is expected to be quite tolerant to a passing saturating signal, both for single and dual polarization lasers. This is clearly confirmed for the dual polarization case in Figs. 6.10 (a) and (c). Also simulation of single polarization lasers (not illustrated here) shows a low sensitivity of the output power to cross-saturation.

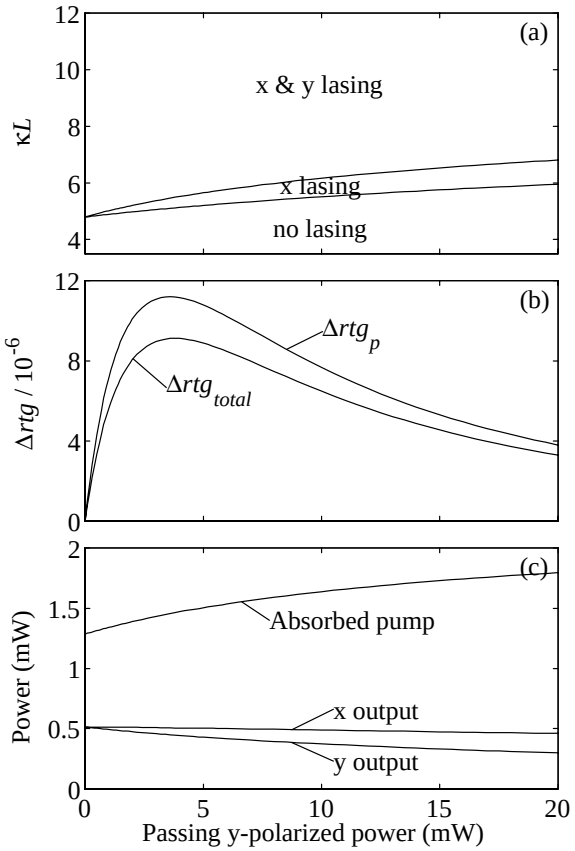

Figure 6.10. Same parameters as in Figure 6.3 plotted against passing cross-saturating power.

Serial multiplexing of DFB lasers should thus be possible as far as mean output power is concerned. This has also been demonstrated experimentally for single polarization lasers in [5] and [31]. Further studies are required to determine what happens to the dynamic behavior in terms of the total intensity noise and intra-modal intensity noise in multiplexed configurations.

The round-trip gain difference contributions in Fig. 6.10 (b) are much lower than in the previous cases (order of 10^{-6} as opposed to 10^{-3}). This is because the passing power does not change the cavity losses significantly.

6.6 Conclusion

A comprehensive model has been presented for multi-moded DFB lasers with arbitrary grating structures, including birefringence, twist and Faraday rotation. The model has been applied to investigate polarization mode competition in fiber lasers with certain polarization imperfections. The magnitudes of the

polarization hole-burning effect and the local and global spatial hole-burning effects have been investigated, and it may be concluded that all these effects are of significance for the polarization mode competition behavior. The laser model may also be used to investigate longitudinal mode competition and fundamental mode thresholds in non-uniform gratings. More experimental work remains to be done to verify the validity of the model.

The grating model presented can also be applied to birefringent passive gratings, and it can readily be extended to include coupling between more than two modes propagating in each direction.

A simple approximation for the polarization dependence of the saturated gain has also been presented, which is believed to be valid both below and above the saturation power P_{sat}. From the approximation we are able to express the polarization dependence of the gain and gain grating parameters in the laser gain medium due to saturation from the laser power, including the standing wave modulation effects.

Promising techniques for achieving single polarization operation seem to be introduction of polarization dependent grating strength, polarization dependent grating phase errors located in the high intensity region of the cavity, twist of the birefringence axes combined with a non-ideal phase-shift, or back reflection into the laser with individually controlled phases for the two polarizations. Since unintended polarization imperfections, like back reflections, may work against the intended imperfections by favoring the mode that is not supposed to be lasing, extra margins should be added to the magnitudes of the intended imperfections.

If a dual polarization laser with stable polarization output power ratio is required, it may be necessary to include an isolator at the laser output to avoid mode competition noise caused by randomly varying back reflection phases.

In general, strong gratings (high κL) are found to be more tolerant to polarization imperfections, and relatively strong gratings should therefore be used when dual polarization lasers are required. There are, however, practical limits to how strong the gratings can be made. First, due to the high Q-factor of DFB's with high κL, even a small intrinsic fiber loss may reduce the slope efficiency significantly. Second, the gain thresholds of all longitudinal modes decrease with increasing grating strength. At the same time the global spatial hole-burning between longitudinal modes increases significantly. This may result in undesired multiple longitudinal mode operation.

Third, due to saturation of the UV-induced index-change, there is a limit to the κ-values that can be achieved. It may not be a good solution to increase κL by increasing L, since the impact of some of the grating imperfections, like twist, polarization dependent chirp, (and also polarization independent chirp) scale proportionally with L. Especially in birefringence sensor applications,

where external forces are supposed to induce birefringence changes, maintaining uniform grating parameters along very long gratings may be difficult.

It is encouraging for sensor applications that serial multiplexing does not seem to affect the static solutions for modal output powers significantly. However, the influence of multiplexing on temporal intensity noise still needs more investigation.

6.7 Acknowledgments

The authors want to thank John Gregory Cowle for fruitful discussions and Kjell Bløtekjær for reading through and commenting the manuscript.

Appendixes:

6.A Background for the PHB Model

Two slightly different models have been presented in the literature for modelling the random orientation of ion cross-section anisotropies. Wysocki et. al. [21] assumes uniaxial gain of each ion, random orientations in three dimensions of the optical axes (OA) of each ion, and identical cross section anisotropies $A = \sigma_\perp/\sigma_\parallel$ for all ions where $\sigma_\perp$ and $\sigma_\parallel$ are the ion cross-sections for fields polarized parallel and orthogonal to the OA. Wagener et. al. [22] uses a simpler model with an "averaged" projected ion anisotropy ϵ, taking random ion orientations in only two dimensions into account. By fitting simulations to measurements of polarization hole-burning (PHB) in erbium doped amplifiers (EDFAs) at moderate signal intensities ($P_s < P_{sat}$), they estimate $A = 0.535$ or 2.17 and $\epsilon = 0.67$, respectively.

For moderate ion anisotropies it is found that (6.7) in Sec. 6.3 can approximate the local PHB calculated with the aforementioned models quite well. When comparing to Wysocki's model with $A = 0.535$ or 2.17, a best fit is obtained with $\eta = 0.059$, as illustrated in Fig. 6.1. For Wagener's model with $\epsilon = 0.67$, a good fit is obtained with $\eta = 0.039$. The difference in estimated η may be due to the fact that the two models are fitted to different experiments, and that Wagener assumes $D_p = 1$ everywhere along the test fiber, thus overestimating the EDFA PHB for the given ϵ.

The polarization dependent gain and gain grating coefficients to be used in the DFB coupled mode equations may be derived from (6.7) along the same lines as was used to derive (6.5) in Sec. 6.3: After expressing the ratio P_s/P_{sat} in (6.7) in terms of its mean value p_{tot} and its standing wave compo-

nent $2Re\left(p_c e^{i\phi}\right)$, Δg and Δg_{gr} are derived as the zeroth and first order Fourier components of $\Delta g_{loc}(\phi)$. This leads to (6.9) in Sec. 6.3.

6.B Gain Medium Contributions to Round-trip Gain

The power transferred to a laser mode from the gain medium per unit length equals $g^r_{eff}|\vec{R}|^2 + g^s_{eff}|\vec{S}|^2$ where g^r_{eff} and g^s_{eff} are the effective power gains contributed to $\vec{R}$ and $\vec{S}$, respectively. By calculating $d|\vec{R}^2|/dz$ and $d|\vec{S}^2|/dz$ from (6.2) and extracting the terms that are due to the gain-medium, the following expressions are obtained:

$$\begin{aligned} g^r_{eff} &= 2\left\{g|r_x|^2 + (g+\Delta g)|r_y|^2 + \mathrm{Re}\left(r_x^* s_x g_{gr}\right)\right. \\ &\quad \left. + \mathrm{Re}\left(r_y^* s_y \left(g_{gr} + \Delta g_{gr}\right)\right)\right\} \left(\left|r_x^2\right| + \left|r_y^2\right|\right)^{-1}, \end{aligned}$$

$$\begin{aligned} g^s_{eff} &= 2\left\{g|s_x|^2 + (g+\Delta g)|s_y|^2 + \mathrm{Re}\left(r_x s_x^* g_{gr}^*\right)\right. \\ &\quad \left. + \mathrm{Re}\left(r_y s_y^* \left(g_{gr}^* + \Delta g_{gr}^*\right)\right)\right\} \left(\left|s_x^2\right| + \left|s_y^2\right|\right)^{-1}. \end{aligned} \tag{6.14}$$

Not all of the power transferred from the gain medium contributes to the round-trip gain. For instance, at the grating ends the only contribution from the gain medium is to amplify the output signals. Numerical investigations indicate that the geometric mean of the forward and backward propagating powers $|\vec{R}(z)|\,|\vec{S}(z)|$ may be used in this context as a good estimate for the fraction of the laser power that is recirculated back into the cavity. The round-trip power contribution in (6.10) is thus calculated as:

$$\begin{aligned} P_{gain} &= \int_0^L \left(g^r_{eff}|\vec{R}(z)|^2 + g^s_{eff}|\vec{S}(z)|^2\right) \\ &\quad \cdot \frac{2\,|\vec{R}(z)|\,|\vec{S}(z)|}{|\vec{R}(z)|^2 + |\vec{S}(z)|^2}\, dz\,. \end{aligned} \tag{6.15}$$

The PHB contribution to rtg_m, and thus Δrtg_p, is found by setting the polarization independent gain parameters g and g_{gr} to zero in (6.14).

The LSHB contribution to rtg_m, and thus Δrtg_l, is obtained as the difference between the actual rtg_m and the value for rtg_m obtained if the standing wave pattern is in exact antiphase with the gain grating, as it will always be in a uniform gain medium with only one laser mode. The latter value is obtained by replacing the $\mathrm{Re}(\cdot)$ function in (6.14) with $-|\cdot|$ (negative absolute value).

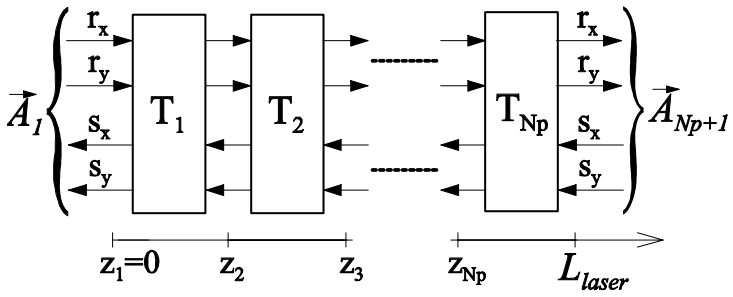

Figure 6.11. Finite element modelling by cascading of 4x4 T-matrixes.

6.C Numerical Model

In the numerical simulations we divide the grating into $q = 1..N_p$ sections along the z propagation axis. Each section may either be a grating section of length Δz_q, in which the coupling matrix $\mathbf{C}_{tot,q}$ is assumed to be constant, or it may be a localized ($\Delta z_q = 0$) perturbation like a phase-shift in the grating structure, reflection, loss or rotation of the birefringence axes.

$N_p = 80$ – 120 sections of variable length were used for the simulations, with shorter sections near the phase-shift position where the intensity and the gain parameters change rapidly. It was verified that further reductions in the section lengths did not give significant changes in the simulation results.

The transfer matrix $\mathbf{T}_q$ of section q is defined by [9]

$$\vec{A}_{q+1} = \mathbf{T}_q \, \vec{A}_q \tag{6.16}$$

where $\vec{A}_q$ is the field amplitude at the left of grating section q. The combined transfer matrix for several cascaded grating sections is computed as the product $\mathbf{T}_{p\cdots q} = \mathbf{T}_q \mathbf{T}_{q-1} \cdot \cdot \mathbf{T}_p$. This cascading of T-matrixes is illustrated in Fig. 6.11.

We assume the coupling parameters to be z-independent within each grating section. For sections with $\Delta z_q > 0$, $\mathbf{T}_q$ may thus be calculated as a product of three matrixes, the first matrix projecting $\vec{A}_q$ into the individual grating modes of (6.3), the second multiplying each mode component by $\exp(-(\gamma_i + i\zeta_i)\Delta z_q)$ and the third doing the reverse projection. This approach is similar to the matrix diagonalization approach presented in [9], and it can be easily extended to evaluate coupling between a larger number of modes.

For a localized perturbation the expression for $\mathbf{T}_q$ may be deduced from well known scattering (S-) matrix expressions [32], [33].

We want to calculate the steady state lasing condition for the DFB laser, taking gain saturation into account, when $m = 1..N_m$ specified modes are lasing. Let δ_m and ε_m denote the detuning and the stored cavity energy of

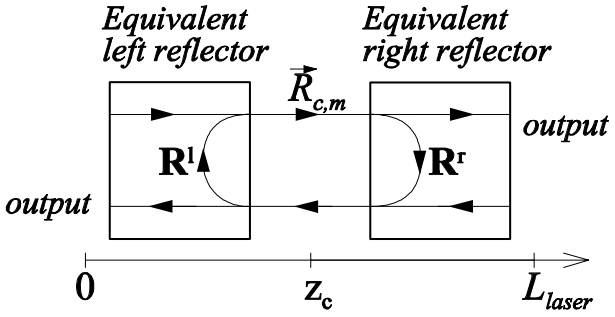

Figure 6.12. Model used for calculating the round-trip Jones-matrix of mode m in eq. (6.17).

mode m. Input parameters to our algorithm are the pump power P_{p0} (launched from left) and initial guesses for:

- the "laser state vector" $\vec{x} = [\varepsilon_1, \ \cdots, \varepsilon_{N_m}, \delta_1, \cdots, \delta_{N_m}]$,
- the right propagating polarization states $\vec{R}_{c,1} \cdots \vec{R}_{c,N_m}$ ($\vec{R}_{c,m} = [r_x, r_y]_m^T$) of each mode at a specified center position z_c, and
- the gain distribution $\mathbf{G}_1 \cdots \mathbf{G}_{N_p}$ ($\mathbf{G}_i$ =gain matrix of the i'th subsection).

The round-trip matrix $\mathbf{RTM}_m$ for each laser frequency is calculated as the product of the effective Jones reflection matrixes at each side of z_c, see Fig. 6.12:

$$\mathbf{RTM}_m = \mathbf{R}^l(\delta_m)\ \mathbf{R}^r(\delta_m). \tag{6.17}$$

$\mathbf{R}^l$ and $\mathbf{R}^r$ are easily computed from the combined T-matrix of each subgrating. Out of the two eigenvalues of $\mathbf{RTM}_m$, the one with a corresponding eigenvector that projects onto $\vec{R}_{c,m}$ is identified as the round-trip gain RTG_m of mode m.

The criterion for a steady state solution is that RTG_m must equal one for all modes. An error gradient algorithm is used that searches for this condition by iteratively calculating improved values for $\vec{x}$ and recomputing the field and gain distributions. The T-matrix formalism outlined above and the gain model outlined in section 6.3 are used for this purpose.

The method outlined may also be adopted for calculating the threshold condition for mode N_m to start lasing, assuming modes $1 \cdots (N_m - 1)$ all have a lower threshold. For instance, the threshold pump power may be computed by assuming $\varepsilon_{N_m} = 0$ while substituting P_{p0} for ε_{N_m} in the definition of $\vec{x}$, i.e. $\vec{x} = [\varepsilon_1, \ \cdots, \varepsilon_{N_m-1}, P_{p0}, \delta_1, \ \cdots, \ \delta_{N_m}]$.

References

[1] J. T. Kringlebotn, J. L. Archambault, L. Reekie and D. N. Payne, Er^{3+}:Yb^{3+}-codoped fiber distributed-feedback laser", *Opt. Lett.*, vol. 19, pp. 2101-2103, 1994.

[2] L. Dong, W. H. Loh, J. E. Caplen, J. D. Minelly and L. Reekie, "Efficient single-frequency fiber-lasers with novel photosensitive Er/Yb optical fibers", *Opt. Lett.*, vol. 22, pp. 694-696, 1997.

[3] W. H. Loh, B. N. Samson, L. Dong, G. J. Cowle and K. Hsu, "Performance Characteristics of Single Frequency Er^{3+}:Yb^{3+} Codoped Fiber Lasers", 1997 *Conf. on Bragg Gratings, Photosensitivity, and Poling in Glass Fibers and Waveguides: Applications and Fundamentals*, sponsored by OSA/ACS, Williamsburg,VA, Tech. Digest vol. 17, pp. 132-134, paper BMC3-1.

[4] J. T. Kringlebotn, W. H. Loh and R. I. Laming, "Polarimetric Er^{3+}-doped fiber distributed-feedback laser sensor for differential pressure and force measurements", *Opt. Lett.*, vol. 21, pp. 1869-1871, 1996.

[5] J. Hübner, P. Varming and M. Kristiansen, "Five wavelength DFB fiber laser source for WDM systems", *Electron. Lett.*, vol. 33, pp. 139-140, 1997.

[6] M. Sejka, P. Varming, J. Hübner and M. Kristiansen, "Distributed feedback Er^{3+}-doped fibre laser", *Electron. Lett.*, vol. 31, pp. 1445-1446, 1995.

[7] H. Storøy, B. Sahlgren and R. Stubbe, "Single polarization fibre DFB laser", *Electron. Lett.*, vol. 33, pp. 56-58, 1997.

[8] H. Kogelnik and C. V. Shank, "Coupled-Wave Theory of Distributed Feedback Lasers", *J. Appl. Phys.*, vol. 43, pp. 2327-2335, 1972.

[9] G. Björk and O. Nilsson, "A New Exact and Efficient Numerical Matrix Theory of Complicated Laser Structures: Properties of Asymmetric Phase-Shifted DFB Lasers", *J. Lightwave Technol.*, vol. LT-5, pp. 140-146, 1987.

[10] M. Yamada and K. Sakuda, "Analysis of almost-periodic feedback slab waveguides via a fundamental matrix-approach", *Appl. Opt.*, vol. 26, pp. 3474-3478, 1987.

[11] G. P. Agrawal, A. H. Robeck, "Modeling of Distributed Feedback Semiconductor Lasers with Axially-Varying Parameters", *IEEE J. Quantum Electron.*, vol. 24, pp. 2407-2414, 1988.

[12] V. C. Lauridsen, T. Søndergaard, P. Varming and J. H. Povlsen, "Design of Distributed Feedback Fibre Lasers" in *Proc. ECOC 97*, vol. 7, paper WE1C, pp. 39-42, 1997.

[13] R. Ulrich and A. Simon, "Polarization optics of twisted single mode fibers", *Appl. Opt.*, vol. 18, pp. 2241-2251, 1979.

[14] J. I. Sakai, T. Kimura, "Birefringence and Polarization Characteristics of Single-Mode Optical Fibers under Elastic Deformations", *IEEE Journal of Quantum Electron.*, vol. QE-17, pp. 1041-1051, 1981.

[15] E. Peral and J. Capmany, "Generalized Block Wave Analysis for Fiber and Waveguide Gratings", *J. Lightwave Thechnol.*, vol. 15, pp. 1295-1302, 1997.

[16] C. R. Giles and E. Desurvire, "Modeling Erbium-Doped Fiber Amplifiers", *J. Lightwave Thechnol.*, vol. 9, pp. 271-283, 1991.

[17] M. Sargent III, W. H. Swantner and J. D. Thomas, "Theory of a Distributed Feedback Laser", *IEEE J. Quantum Electron.*, vol. QE-16, pp. 465-472, 1980.

[18] W. S. Rabinovich and B. J. Feldman, "Spatial Hole Burning Effect in Distributed Feedback Lasers", *IEEE J. Quantum Electron.*, vol. 25, pp. 20-30, 1989.

[19] V. J. Mazurczyk and J. L. Zyskind, "Polarization Dependent Gain in Erbium Doped-fiber Amplifiers", *IEEE Photon. Technol. Lett.*, vol. 6, pp. 616-618, 1994.

[20] V. J. Mazurczyk, R. H. Stolen, J.-S. Wang and C. D. Poole, "Observation of polarization hole burning in Er-doped fiber for circular polarization of the saturating signal", *1995 Conference on Optical Fiber Communications, Tech. Dig.*, pp. 49-50, paper TuJ7.

[21] P. Wysocki and V. Mazurczyk, "Polarization Dependent Gain in Erbium-doped Fiber Amplifiers: Computer Model and Approximate Formulas", *J. Lightwave Thechnol.*, vol. 14, pp. 572-584, 1996.

[22] J. L. Wagener, D. G. Falquier, M. J. Digonet, H. J. Shaw, "A Muller Matrix Formalism for Modelling Polarization Effects in Erbium-Doped Fiber", *J. Lightwave Thechnol.*, vol. 16, pp. 200-206, 1998.

[23] T. Erdogan and V. Mizrahi, "Characterization of UV-induced birefringence in photosensitive Ge-doped silica optical fibers", *J. Opt. Soc. Amer. B*, vol. 10, pp. 2100-2105, 1994.

[24] P. Niay, P. Bernage, T. Taunay, M. Douay, E. Delevaque, S. Boj and B. Poumellec, "Polarization Selectivity of Gratings Written in Hi-Bi Fibers by the External Method", *IEEE Photon. Technol. Lett.*, vol. 7, pp. 391-3, 1995.

[25] K. Okamoto, T. Hosaka, T. Edahiro, "Stress Analysis of Optical Fibers by a Finite Element Method", *IEEE J. Quantum Electron.*, vol. QE-17, pp. 2123-2129, 1981.

[26] Y. Namihira, "Opto-Elastic Constant in Single Mode Optical Fibers", *J. Lightwave Thechnol.* vol. LT-3, pp. 1078-1083, 1985.

[27] R. B. Wagreich, W. A. Atia, H. Singh and J. S. Sirkis, "Effects of diametric load on fibre Bragg gratings fabricated in low birefringent fibre", *Electron. Lett.*, vol. 32, pp. 1223-1224, 1996.

[28] L. Bjerkan, K. Johannessen, X. Guo, "Measurement of Bragg Grating birefringence due to transverse compressive forces" in *1997 Optical Fiber Sensors Conference,* Williamsburg, VA, Tech. Dig. vol. 16, paper OTuC7-1.

[29] Z. E. Haratjunian, W. H. Loh, R. I. Laming and D. N. Payne, "Single polarization twisted distributed feedback fibre laser", *Electron. Lett.*, vol. 32, pp. 346-348, 1996.

[30] H. Y. Kim, S. K. Kim, H. J. Jeong, H. K. Kim and B. Y. Kim, "Polarization properties of a twisted fiber laser", *Opt. Lett.*, vol. 20, pp. 386-388, 1995.

[31] K. P. Koo and A. D. Kersey, "Noise and cross talk of a 4-element serial fiber laser sensor array", in *1996 Conf. on Optical Fiber Communications*, paper ThP2, Tech. Dig., pp. 266-267.

[32] Y. Weissman, *Optical Network Theory.* Bostaon, MA: Archtech House, 1992, pp. 33-44.

[33] A. Yu and A. S. Siddiqui, "Systematic method for the analysis of optical fibre circuits", *Proc. Inst Elec. Eng.*, vol. 142, pp. 165-175, 1995.

Chapter 7

Polarization Characteristics of Fiber DFB Lasers Related to Sensing Applications[1]

Abstract — An experimental and theoretical investigation of dual polarization Er-doped fiber DFB lasers, and how the polarization mode competition and polarization beat frequency depend on localized transverse force perturbations, back reflections, or changes in pump polarization state is reported. Good agreement between the experiments and a comprehensive theoretical model is obtained. Use of a dual polarization laser as a transverse force sensor with a resolution in the order of 1–100 nN/$\sqrt{\text{Hz}}$ above 20 Hz is also discussed.

Index Terms — Fiber lasers, DFB lasers, Laser mode competition, Gain hole-burning, Optical fiber sensors.

7.1 Introduction

Fiber distributed feedback (DFB) lasers are attractive devices for both for telecommunication and sensing applications [1, 2, 3], due to their narrow linewidth, robust single longitudinal mode operation, compact in-fiber design, flexible and accurate wavelength selection in production, as well as easy tuning of the wavelength.

Robust single polarization sources are generally required for interrogation of interferometric and Bragg grating fiber sensors, as well as in telecommunication applications. A single polarization fiber DFB laser may also be used as a very

[1]Manuscript accepted for publication in Journal of Quantum Electronics. Minor revisions will be made prior to publication. Authors: Erlend Rønnekleiv, Morten Ibsen, and Gregory J. Cowle.

sensitive sensor element on its own, as the laser frequency is sensitive to strain, temperature and other perturbations that change the optical period of the DFB grating. Two methods for ensuring single polarization operation have been reported experimentally, which exploit the polarization dependence of the UV-induced index change. One is based on extra UV-exposure of a grating section to produce a distributed birefringent grating phase-shift [4, 5]. The other is based on inducing a polarization dependence of the grating coupling coefficient κ [6]. Another method reported in [7] is based on twisting a dual polarization fiber DFB laser to make it single polarization.

The polarization beat frequency of dual polarization fiber DFB lasers is sensitive to perturbations that change the fiber birefringence, such as temperature or lateral forces. Simultaneous monitoring of the beat and laser frequencies from such lasers allows for single point dual parameter sensors such as the force-temperature sensor demonstrated in [2] or the strain-temperature sensor demonstrated in [3]. For these applications, robust dual polarization operation of the laser is required.

In both single and dual polarization sensing applications the need for a direct physical contact or interaction between the laser and the measurand may lead to non-uniform birefringence along the DFB structure, which may in turn affect the polarization mode competition (PMC) within the laser. External back reflections and the state of polarization (SOP) of the pump are also expected to affect the PMC behavior of the lasers. In addition, back reflections will affect the polarization beat frequency. Many sensing applications will not allow the fiber laser sensor to be located close to the pump laser and optical isolators. Control with the pump SOP launched into the laser may therefore not be realistic, and isolation against external back reflections may be relatively poor. It is expected that problems due to drift in the pump SOP can be reduced or eliminated by scrambling the pump polarization. However, a polarization scrambling component would increase the complexity and cost of a sensor interrogation system, and it is therefore of interest to know if a sensor system can be operated without such scrambling.

The above mentioned problems call for a quantitative understanding of the mechanisms governing the PMC behavior and polarization beat frequency fluctuations in fiber DFB lasers. A comprehensive theoretical model was developed in [8] and several examples discussing the PMC behavior was given. One purpose of the present work is to verify the model experimentally, and to extend it to also cover pump induced polarization dependent gain (PDG). A further purpose is to investigate the dependence of the polarization beat frequency on localized lateral forces and external reflections. These investigations can reveal useful insight into the obtainable sensitivity for polarimetric fiber DFB laser

sensors to lateral forces and the limitations set by external back reflection to the accuracy of polarimetric fiber DFB laser sensors in general.

7.2 The Investigated Lasers

Two dual polarization fiber DFB lasers operating at 1549 nm, in the following denoted DFBa and DFBb, have been investigated. The lasers consist of two consecutive uniform subgratings of lengths L_1 and L_2 with a localized π grating phase-shift in between. DFBa is symmetric with $L_1 = L_2 = 20$ mm, while DFBb is asymmetric with $L_1 = 17.4$ mm and $L_2 = 25$ mm. Both lasers were characterized with a heat perturbation technique in [9], verifying fundamental longitudinal mode operation and a grating coupling parameter of $\kappa = 230$ m^{-1} $\pm 10\%$. In [9], DFBa and DFBb were named "laser #1" and "laser #3", respectively.

DFBa produced an output power of 205 μW $\pm 10\%$ in each direction when pumped from either end by 83 mW of 1480-nm pump power. Under the same pumping conditions, the asymmetric DFBb produced 395 μW $\pm 10\%$ from output port 1 (grating section L_1), and 11.5 μW $\pm 10\%$ from port 2 (grating section L_2).

The laser gratings were produced by UV exposure of a D_2-loaded fiber with an Er-Yb-doped core and a UV-sensitized B-Ge-doped ring outside the core [10]. Before UV exposure, but after D_2-loading of the fiber, the fiber transmission spectrum was measured for various pump powers. From these measurements, the absorption (a_x) and gain (g_x) coefficients at zero and full inversion, respectively, at the laser signal ($x = s$) and pump ($x = p$) wavelengths were found to be $[a_s, a_p, g_s, g_p] = [11.7, 8.9, 15.9, 3.0]$ dB/m. The spontaneous emission power at full inversion was $P_{sp} = 4.1$ mW/m.

Fitting of simulations to the measured slope efficiency of DFBa published in [11] indicates that the lifetime of a fraction $\xi = 38$ % of the Er-ions have been reduced (quenched) by a factor $\zeta = 26$ during the UV-exposure. In addition, an unbleachable loss of $a_0 = 0.24$ dB/m seems to be present. UV-induced quenching in Er^{3+}-doped glasses has earlier been reported in [12]. The slope efficiency of DFBb has also been measured, indicating very similar parameters for that laser: $\xi = 39$ %, $\zeta = 25$, and $a_0 = 0.24$ dB/m.

7.3 Response to Transverse Force

A polarization dependent phase-shift may be introduced in a fiber by applying a transverse force, resulting in stress-induced birefringence. We have investigated the sensitivity to transverse forces for a section of the same fiber that DFBa

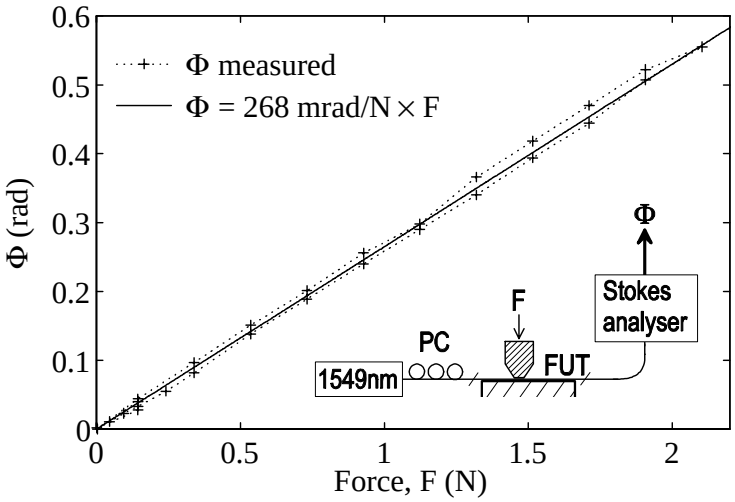

Figure 7.1. Polarization dependent phase shift Φ versus transversal force F applied to a section of the fiber used for the laser production. The measurement setup is illustrated in the inset drawing. PC, polarization controller.

and DFBb were made from, using the setup illustrated in the inset of Fig. 7.1. A variable force F was applied to a 1 mm section of the fiber under test (FUT). Polarized light at 1549 nm was launched from one end, and the resulting output SOP was monitored by a Stokes analyzer. After adjusting the input SOP so that the output SOP had maximum sensivity to the applied force, the difference Φ between the force-induced phase-shifts for optical fields polarized parallel and orthogonal to the force could be measured as the angular rotation of the output SOP on the Poincarè sphere. The result of this experiment is plotted in Fig. 7.1, showing a force sensitivity of $\Phi/F = 0.268 \pm 0.005$ rad/N. This value is somewhat less than the 0.29 rad/N indicated theoretically for silica fiber in [13] and experimentally in [2]. The hysteresis observed in Fig. 7.1 of ~ 70 mN may be due to hysteresis in the force monitoring arrangement.

Fig. 7.2 shows the setup used to investigate the sensitivity of DFBb to a polarization-dependent phase-shift induced by pressing on a ~ 1 mm section of the laser fiber close to the position of the permanent grating phase-shift. 83 mW of 1480-nm polarized pump power was launched into port 1 of the laser via a polarization controller (PC1) and a 1480 – 1550 nm wavelength division multiplexer (WDM). The laser output from port 1 was guided via the 1550-nm branch of the WDM through an isolator (ISO), a polarization controller (PC2) and a polarizing beam-splitter (PBS) to detectors Dx and Dy. To be able to monitor the PMC behavior of the laser, PC2 was adjusted so that Dx and Dy monitored the output powers P_x and P_y from the x- and y- laser polarization

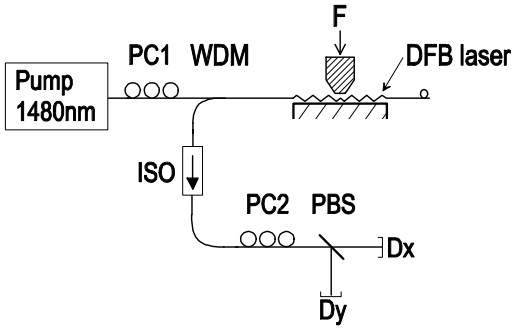

Figure 7.2. Setup for investigation of the laser response to a transverse force F applied near the grating phase-sift position.

modes, respectively. The given values for P_x and P_y have been corrected for losses measured between the laser output and the detector. Measurements were also made of the force-induced frequency shifts $\Delta\nu_x$ and $\Delta\nu_y$ of the x and y laser modes and the polarization beat frequency $\nu_b = |\Delta\nu_x - \Delta\nu_y|$. These frequency measurements were made by replacing Dx with a high finesse Fabry-Perot optical spectrum analyzer and connecting an RF spectrum analyzer to Dy. The state of PC2 was then adjusted so that the laser polarizations were mixed in the PBS, causing two separated peaks at the optical spectrum analyzer, and a distinct peak at the polarization beat frequency at the RF spectrum analyzer.

The measurements were first performed with the force applied parallel to the x polarization axis of the laser, and then repeated with the force parallel to the y polarization axis. The applied forces will be denoted F_x and F_y for the two cases, respectively. For each direction of the force, the modal output powers P_x and P_y were recorded versus the applied force. This measurement was repeated with PC1 adjusted first for maximum in P_x and then for maximum in P_y, corresponding to x and y polarized pump, respectively. Recordings of $\Delta\nu_x$, $\Delta\nu_y$ and ν_b versus the applied forces were also made.

Note that the direction of the x and y polarization states in the laser could not be measured directly in the experiment, due to random changes of polarization states between the laser and the PBS. The identification of the modes is therefore based on theoretical calculations of the birefringence due to transverse forces [13], from which we find that $\Delta\nu_x - \Delta\nu_y$ should increase with F_x and decrease with F_y.

Fig. 7.3 (a) shows the measured (markers) $\Delta\nu_x$, $\Delta\nu_y$ and $\Delta\nu_x - \Delta\nu_y$ versus F_x and F_y. No significant dependence on the pump polarization could be observed in the frequency measurements. For an ideal DFB laser grating, the frequency shift of mode $q = x, y$ due to a locally induced grating phase shift $\Delta\phi_q$ in the

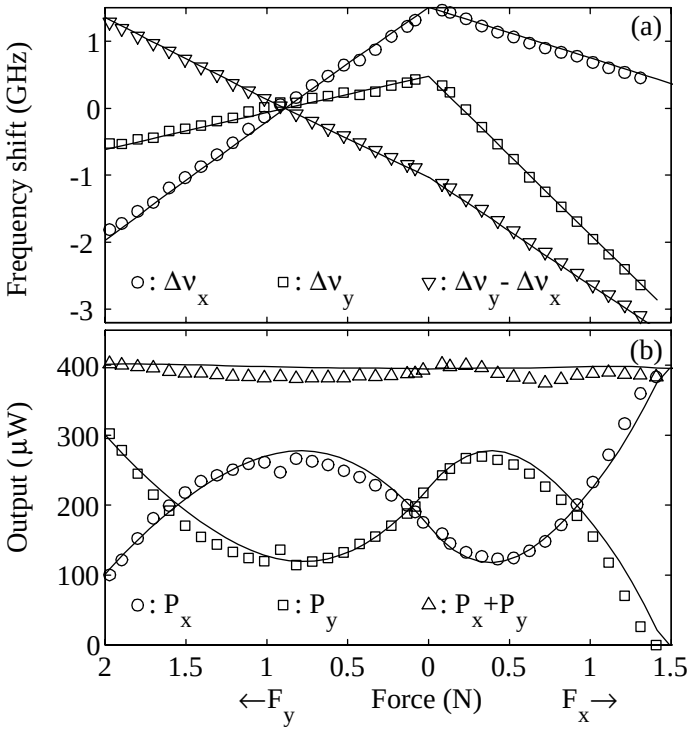

Figure 7.3. (a) Frequeny shifts $\Delta\nu_x$ and $\Delta\nu_y$, and polarization beat frequency $\Delta\nu_y - \Delta\nu_x$, plotted versus transverse force F_x or F_y applied parallel to the x or y birefringence axes of DFBb, respectively (c.f. Fig. 7.2). Responses to F_x are shown to the right and responses to F_y to the left. (b) Output powers P_x, P_y, and total output $P_x + P_y$. Markers and lines illustrate measurements and simulations, respectively.

q polarization propagation mode may be expressed as [9]:

$$\Delta\nu_q = -\frac{\kappa c}{4\pi n} \exp\left(-2\kappa|z|\right)\, \Delta\phi_q \tag{7.1}$$

Here, $c\kappa/(2n)$ is the inverse round-trip delay of the laser cavity at the grating phase-shift position $z = 0$, c is the speed of light in vacuum, n is the refractive index of the fiber, κ is the grating coupling coefficient, and $\exp(-2\kappa|z|)$ is the laser intensity dependence on the distance z from the grating phase-shift. The measured beat frequencies satisfy $d(\Delta\nu_y - \Delta\nu_x)/dF_x \approx -1.60$ GHz/N and $d(\Delta\nu_y - \Delta\nu_x)/dF_y \approx 1.16$ GHz/N. Taking into account that the forces are distributed over a 1 mm length and assuming $\kappa = 230$ m^{-1}, $n = 1.465$, and $|\Delta\phi_y - \Delta\phi_x| = 2\Phi = 0.536$ rad/N $\times F_q$ from Fig. 7.1, this indicates that F_x and F_y have been centered at effective distances $z = 0.5$ and 1.25 mm from the permanent π phase-shift position, respectively.

From the measured frequency shifts $\Delta\nu_x$ and $\Delta\nu_y$ of the individual modes and from (7.1), we estimate the sensitivity of the grating phase-shift to transverse force in the direction parallel to the optical polarization to be $k_{\|} = \Delta\phi_x/F_x = \Delta\phi_y/F_y = 0.255 \pm 0.04$ rad/N, and the sensitivity to orthogonal forces to $k_{\perp} = \Delta\phi_y/F_x = \Delta\phi_x/F_y = 0.791 \pm 0.04$ rad/N. Theoretical expressions for the sensitivities of the fiber refractive indices to transverse forces were derived by Sakai and Kimura in [13]. However, they did only take into account transverse stresses in the fiber, while effects of axial (z-directed) stress or strain were ignored. When we take these effects into account and use the same material parameters as in [13], we obtain $[k_{\|}, k_{\perp}] = [-0.031, 0.543]$ rad/N for a fiber that is axially constrained (no z-directed strain) and $[k_{\|}, k_{\perp}] = [0.175, 0.747]$ rad/N for a fiber that free to expand axially. As seen from the results, axial strain causes a polarization independent offset to $[k_{\|}, k_{\perp}]$. Our measurements indicate that this offset is even higher than calculated for the free axial expansion case. This high offset may be due to z-directed stress in the 1 mm long plastic surface (overhead copier grade foil) that was used to transfer the force to the fiber. If the transverse force is applied from relatively stiff surfaces over a longer length of the fiber, less axial strain is expected. This expectation is confirmed by results reported by Wagreich *et. al.* [14] from pressing on a 25 mm fiber section with a passive grating Bragg between polished aluminum plates. Their results correspond to $[k_{\|}, k_{\perp}] = [0.10 \pm 0.07,\ 0.62 \pm 0.15]$ rad/N at 1550 nm, which is close to what is expected theoretically for the axially constrained case.

The beat frequency measurements in Fig. 7.3 (a) demonstrates that the arrangement in Fig. 7.2 could be used as a very sensitive transverse force sensor. Dual polarization fiber DFB lasers used as transverse force sensors were first demonstrated in [2] by pressing on the full length of a 100 mm laser, producing a sensitivity of 96 MHz/N. The higher sensitivity of 1.6 GHz/N obtained here is due to the concentration of the force near the most sensitive region of the laser. Measurements of the fluctuations in ν_b when no perturbations were applied have been made for DFBa using a setup that will be described in the Sec. 7.4. Fig. 7.4 shows the noise spectral density $\nu_{b,rms}$ of the beat frequency versus interrogation frequency f. $\nu_{b,rms}$ decrease from 120 Hz/$\sqrt{\text{Hz}}$ at $f = 20$ Hz to 2.1 Hz/$\sqrt{\text{Hz}}$ at $f = 40$ kHz. In a sensor with a sensitivity of 1.6 GHz/N these noise levels would produce a noise floor (noise equivalent force) ranging from 75 to 1.3 nN/$\sqrt{\text{Hz}}$ in the same frequency interval, as illustrated by the right-hand axis in Fig. 7.4. The origin of $\nu_{b,rms}$ is not known, but it may be related to time varying back reflections to the laser, as will be discussed in Sec. 7.4.

Fig. 7.3 (b) illustrates the measured (markers) P_x, P_y and $P_x + P_y$ averaged over the two pump polarizations, and is believed to be representative for a situation with a scrambled pump polarization. Pump polarization dependence

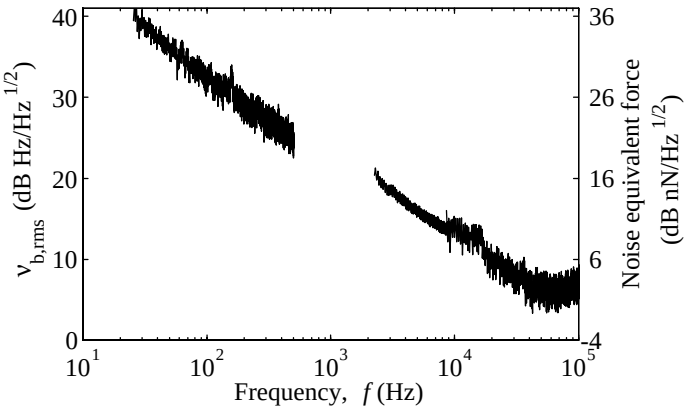

Figure 7.4. Measured beat frequency noise $\nu_{b,rms}$ for DFBa. The right-hand axis shows the corresponding noise equivalent force for a transverse force sensor.

will be discussed in Sec. 7.5. The total output power $P_x + P_y$ is seen to be fairly independent on F_x and F_y. The modal power difference $P_x - P_y$ decreases with F_x to a minimum at $F_x = 0.4$ N, and then increases until only the x-polarization is lasing at $F_x = 1.4$ N. The dependence on F_y is very similar, except for a sign-shift in $P_x - P_y$. This observed dependencies of P_x and P_y on F_x and F_y may be explained by assuming a negative polarization independent grating phase-shift error near $z = 0$. When a force is applied, this error is compensated most efficiently for the polarization axis orthogonal to the force (since $k_\perp > k_\parallel$), and the output power of the corresponding laser mode is favored. The mode polarized parallel to the force starts taking over about when the phase-shift error of the orthogonal mode is fully compensated near $F_x = 0.4$ or $F_y = 0.8$ N, and starts to increase in absolute value.

A complete degeneration of the laser modes as ν_b approached zero was not observed. Instead, ν_b went through a minimum value of $\nu_b \approx 14$ MHz at $F_y \approx 0.89$ N, while the polarization states of the laser modes were continuously transformed to their respective orthogonal states. This behavior may be explained by a small ($<2^\circ$) misalignment between F_y and the birefringence axis, and is the explanation for the irregularities in the measured P_x and P_y near $F_y = 0.89$ N.

The lines in Fig. 7.3 (a) and (b) show simulation results obtained using the model described in Appendix 7.A and [8]. A depolarized pump ($D_{pp} = 0$) was assumed, and the polarization hole-burning (PHB) parameter was set to $\eta = 0.12$. The grating and gain parameters were assumed as described above, except for bias grating phase-shifts in the x and y polarization modes of $\Delta\phi_{x0} = -0.20$ rad and $\Delta\phi_{y0} = -0.18$ rad, respectively, which were added to the nominal π phase-shift at $z = 0$. Small adjustments were also made

to ξ, ζ, and a_0 to maintain a good fit with the measured slope efficiency at $F_x = F_y = 0$. We see that the model produces a good fit to the measurements in Fig. 7.3. The model parameters that have been fitted to the measurements in Fig. 7.3 may be summarized as the force positions and the offset in $[k_\parallel, k_\perp]$ which are determined by the slopes of $\Delta\nu_x$ and $\Delta\nu_y$, $\Delta\phi_{x0}$ and $\Delta\phi_{y0}$ which are determined by the local maximum and minimum in $P_x - P_y$ and the offset in $P_x - P_y$ at $F_x = F_y = 0$, and η which is determined by the magnitude of $P_x - P_y$.

The observed local maxima and minima in $P_x - P_y$ could in principle be explained by assuming a UV-induced gain grating, which would be in phase with the index grating, instead of the bias grating phase errors. Such an effect would arise because the force-induced phase-shifts would cause the overlap between the standing wave intensity pattern and the gain grating to vary differently for the two laser polarizations. A UV-induced gain grating could either come from modulation of the unbleachable losses a_0 or modulations of the lifetime-quenched ion fraction ξ. However, the grating modulation amplitudes cannot exceed the estimated mean values for a_0 and ξ since negative background losses or ion fractions are not realistic. Simulations have shown that even with the maximum possible modulation amplitudes, bias phase-shifts $\Delta\phi_{x0}$ and $\Delta\phi_{y0}$ in the order of -0.12 rad must be assumed to achieve good fit with the measurements.

7.4 Response to External Back Reflections

Fig. 7.5 shows the setup used to investigate the sensitivity of DFBa and DFBb to back-reflections. 83 mW of 1480-nm pump was supplied to the laser through PC1 and the WDM in the same way as for the experiment in Fig. 7.2. Back-reflection into the forward port (right-hand side in figure) of the laser with variable attenuation, optical phase-shift and polarization state was generated by use of a variable attenuator (VA), a piezo-electric fiber stretcher (PZT) modulated at ~ 8 Hz by a function generator (F.gen.), a polarization controller (PC3), and a fiber end reflector (Refl.). A 10:90 coupler was inserted between the laser and the VA, and by connecting fiber connectors FC2 and FC3 the forward output power could be monitored through the 10% output port from the coupler. Alternatively, the backward output could be monitored through the WDM and isolator ISO1 by connecting FC1 to FC3. In the latter case FC2 was terminated with a fiber bend to avoid reflections. The detection system with ISO2, PC2, PBS, Dx and Dy is identical to that shown in Fig. 7.2, except for a tunable optical band-pass filter (BPF) with 1 nm bandwidth inserted between PC2 and the PBS to stop pump power from reaching the detectors.

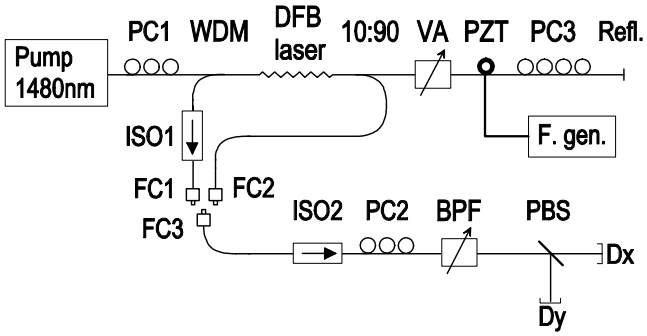

Figure 7.5. Setup for investigation of the laser polarization mode responses to back-reflections.

The observed dependencies of the modal output powers P_x and P_y on the dual-pass phase modulation Φ_{PZT} induced by the PZT was in agreement with the theoretically expected dependencies, indicated by the solid lines in Fig. 7.6. We maximized the amplitude of $P_x - P_y$ by adjusting PC3. It is believed that this corresponds to back reflection phases in the x and y polarizations that differ by π, while the reflected state of polarization is preserved for both laser modes. Thus, when Φ_{PZT} causes constructive interference between back reflected and intracavity signals for one mode, the other mode experiences destructive interference, and vice versa. The minima and maxima in output power versus Φ_{PZT}, denoted $P_{q,r,max}$ and $P_{q,r,min}$ where $q = x, y$ is the laser mode index, were then recorded as a function of back reflection level. This experiment was first performed with x-polarized pump ($r = x$) and then with y-polarized pump ($r = y$). To remove the pump polarization dependence, intrinsic differences in laser mode efficiencies, as well as polarization dependent measurement errors, we will in this section illustrate the averaged values $P_{max} = \overline{P_{q,r,max}}$ and $P_{min} = \overline{P_{q,r,min}}$, where the averages are taken over all possible combinations of q and r.

The markers in Figs. 7.7 (a) and (b) show the measured P_{max}, P_{min}, and $P_{max} + P_{min}$ plotted against back reflection level for the symmetric laser DFBa. (a) and (b) illustrate measurements made through the forward (FC2) and backward (FC1) ports, respectively. The PMC behavior is similar for the two directions, with P_{min}/P_{max} decreasing from >0.94 at <-55 dB reflection to zero at -24 dB.

The lines in Figs. 7.7 (a) and (b) show the simulated laser behavior, assuming phase and polarization of the back reflections as described above, depolarized pump ($D_{pp} = 0$), $\eta = 0.12$, and otherwise the parameters given for DFBa in Sec. 7.2. It can be seen that the agreement between measurements and simulations is good.

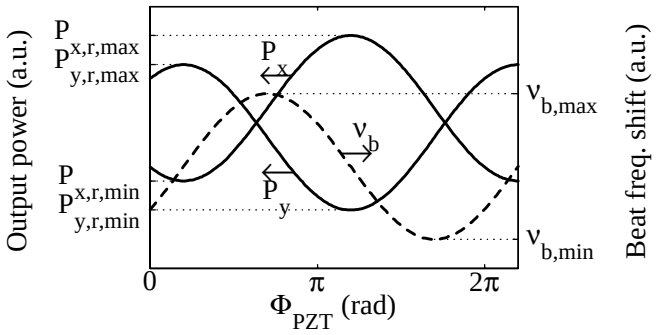

Figure 7.6. Dependence of modal powers P_x, P_y and the polarization beat frequency shift $\Delta\nu_b$ on the external cavity roundtrip phase-shift Φ_{PZT} induced by the PZT.

For polarimetric laser sensors relying on accurate readout of the polarization beat frequency ν_b, back reflection induced shifts in ν_b may contribute to measurement errors. We measured the back-reflection induced beat frequency shift for DFBa by adjusting PC2 so that the beat signal at $\nu_b \approx 970$ MHz was received at Dx (c.f. Fig. 7.5). The beat frequency was shifted down in an electronic mixer and passed to a 0-2 MHz frequency to voltage converter. The resulting voltage, monitored on an oscilloscope, was similar to the dashed line in Fig. 7.6. Fig. 7.7 (c) shows the measured (markers with error bars) and simulated (line) peak-to-peak beat frequency shift $\Delta\nu_b = \nu_{b,max} - \nu_{b,min}$. We see that $\Delta\nu_b$ exceeds the short term ($\sim$5 s) beat frequency drift of $\Delta\nu_b = \pm 10$ kHz observed in [3] when the back reflection level is > -50 dB. Rayleigh back scattering from ~ 60 m of standard single mode fiber is sufficient to produce this back reflection level. The observed beat frequency drift could, however, also be due to random temperature fluctuations or bad isolation against discrete reflectors. If the laser is used as a transverse force sensor or as a temperature sensor [3], $\Delta\nu_b = \pm 10$ kHz would correspond to readout errors of ± 6 μN or ± 6 mK, respectively.

The noise floor $\nu_{b,rms}$ at higher interrogation frequencies, seen in Fig. 7.4, may also be due to unintended back reflections with random phase. Fluctuations in back reflection phase can be caused by fluctuations in the mean laser frequency or by thermally or mechanically induced fluctuations in the optical path lengths to the reflecting points.

$\Delta\nu_b$ may be approximated analytically by:

$$\Delta\nu_b = \nu_{b,max} - \nu_{b,min} \simeq \frac{\kappa c}{\pi n} rT \left(1 + \alpha_B^2\right)^{1/2}, \tag{7.2}$$

where r is the external amplitude reflectivity, T is the power transmissivity of the grating section (or laser mirror) between r and the DFB phase-shift position, $\alpha_B = \delta(\Delta\phi_x - \Delta\phi_y)/\delta\Delta rtg_{total}$ is the linewidth enhancement factor for the beat frequency, and $\delta(\Delta\phi_x - \Delta\phi_y)$ and $\delta\Delta rtg_{total}$ are changes in

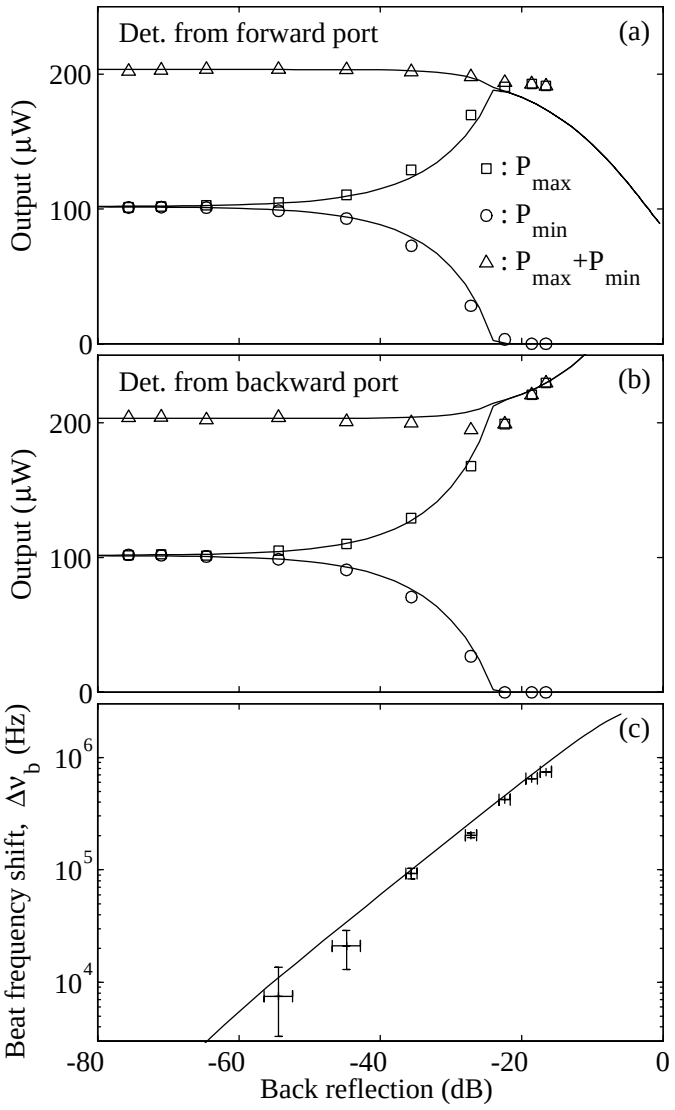

Figure 7.7. Measured (markers) and simulated (lines) response of DFBa to back-reflection into the forward port (c.f. Fig. 7.5). (a) and (b) illustrate modal output powers from the forward and backward ports, respectively. (c) shows the peak to peak modulation of the polarization beat frequency.

the polarization dependencies of the grating phase shift and the cavity roundtrip amplitude gain [8a], respectively, due to PHB. $T \simeq 4\exp(-2\kappa L_1)$ for an ideal grating section of length L_1. (7.2) is a valid approximation provided that $rT \ll 1$ (weak reflection), $\pi\Delta\nu_b\tau_{ext} \lesssim 1$ (no external cavity-mode hopping) where τ_{ext} is the external cavity roundtrip time, and $\tau_{ext} \ll \tau_{coh}$ where τ_{coh} is the laser coherence time. All these conditions were satisfied in our experiment. For our gain medium α_B is not known, and $\alpha_B = 0$ was therefore assumed for the simulations in Fig. 7.7 (c). The discrepancy between simulations and measurements indicates that the actual rT-product may have been 10 to 40 % higher than the value used for the simulations, corresponding to an underestimate of κL_1 by 1 to 4 %. This estimation error is well within the ±10 % uncertainty of the κ measurement [9].

Fig. 7.8 shows the measured (markers) and simulated (lines) response of DFBb to back reflections. (a) and (b) illustrate outputs from port 1 and 2, respectively, with back reflection into port 1. (c) illustrates output from port 1 with back reflection into port 2. The simulation parameters are the same as in Fig. 7.2. Again, the agreement between simulations and measurements is seen to be good.

The ratio T_1/T_2 of the laser mirror transmissivities of DFBb at port 1 and 2 equals the port 1 to port 2 output power ratio of 15 dB. The curves in Fig. 7.8 (c) are shifted by approximately two times this ratio (30 dB) relative to the curves in Figs. 7.8 (a) and (b). Thus, the PMC behavior is similar when the power fraction reflected back into the cavity is similar, i.e. $(rT_1)^2 = (rT_2)^2$. Note, however, that this relation is valid only when comparing the sensitivities of one laser to back reflection through two different ports. The tolerable back reflection into either port is not generally expected to drop so efficiently if both T_1 and T_2 are reduced simultaneously. This is because a reduced cavity loss implies an increase in the intensity inside the cavity, while the PHB effect is expected to decrease with increasing signal intensity [8b].

The minimum output degree of polarization (DOP) $(P_{max} - P_{min})/(P_{max} + P_{min})$ is seen from Figs. 7.7 and 7.8 to be fairly independent on output direction for both DFBa and DFBb. This observation illustrates that the relative change of the output transmissivities for the two modes caused by the back reflection is small within the dual polarization regime.

7.5 Dependence on Pump Polarization

The markers in Fig. 7.9 show the measured pump polarization dependence of the transverse force measurements that were first presented in Fig. 7.3 (b). The solid and dashed lines show simulation results obtained when we assume an effective pump PHB parameter of $\eta_p = 0.021$ and otherwise simulation

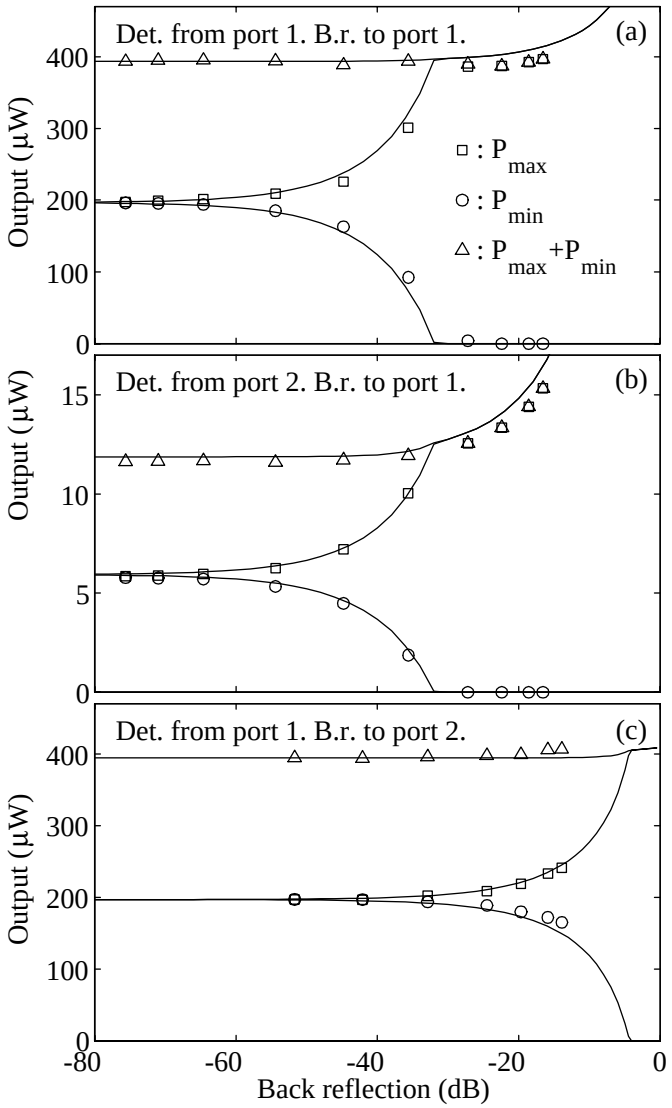

Figure 7.8. Measured (markers) and simulated (lines) response of DFBb to back-reflections (c.f. Fig. 7.8). The monitored port and the port experiencing back reflections are indicated in each sub-figure.

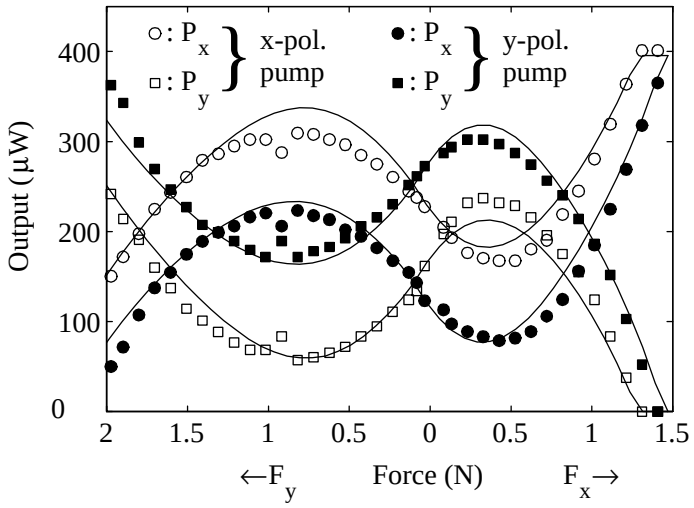

Figure 7.9. Pump polarization dependence of the measurements in Fig. 7.3 (b). Open and filled markers illustrate measurements with the pump aligned with the x and y polarizations, respectively.

parameters that are identical to those used in Fig. 7.3 (including $\eta = 0.12$). We see that the pump PHB model produces fairly good agreement with the measurements.

The markers in Fig. 7.10 show the measured pump polarization dependence of the back reflection measurements that were first presented in Fig. 7.7 (a). The open markers show $P_{q,r,max}$ and $P_{q,r,min}$ (c.f. Fig. 7.6), averaged over all possible combinations (q, r) where the mode r favored by the pump polarization is identical to the mode favored by the back reflection (q for P_{max} and opposite of q for P_{min}), i.e.: $P_{max} = (P_{x,x,max} + P_{y,y,max})/2$ and $P_{min} = (P_{y,x,min} + P_{x,y,min})/2$. The filled markers illustrate the opposite situation when the pump polarization and back reflection favor different modes, i.e.: $P_{max} = (P_{x,y,max} + P_{y,x,max})/2$ and $P_{min} = (P_{x,x,min} + P_{y,y,min})/2$. This averaging should eliminate effects of intrinsic differences in laser mode efficiencies, as well as polarization dependent measurement errors. The lines in Fig. 7.10 show the simulation results obtained with $\eta_p = 0.021$ and otherwise identical parameters to those used in Fig. 7.8 (including $\eta = 0.12$). Again, there is good agreement between theory and measurements.

The pump polarization dependencies of the remaining back reflection measurements, first presented in Figs. 7.7 (b) and 7.8 (a,b,c), were also found to be in good agreement with the simulations.

The PHB model used for the simulations is described in Appendix 7.A. It is based on an ion anisotropy model described in [15] where the Er ions are assumed to have uniaxial gain, random orientation of their optical axes (OA)

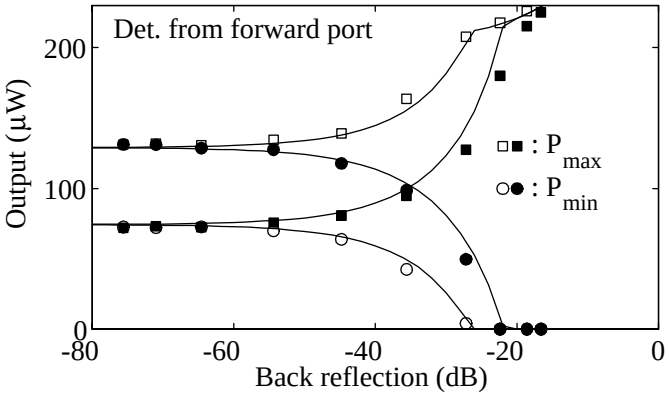

Figure 7.10. Pump polarization dependence of the measurements in Fig. 7.7 (a). Open and filled markers illustrate measurements with the pump aligned with the laser mode that is favored and disfavored by the back-reflection, respectively.

and ion cross section anisotropies defined by $A = \sigma_\perp/\sigma_\parallel$, $\sigma_\perp$ and $\sigma_\parallel$ being the ion cross-sections for fields polarized parallel and orthogonal to the OA. $\eta_p = \eta$ would be expected if the ion anisotropies were identical at the pump and signal wavelengths. However, our measurements indicate $\eta_p \approx 0.18\eta$. This reduced sensitivity to pump PHB may be due to a cross-section anisotropy that is closer to $A = 1$ at 1480 nm than at 1549 nm, or to a low correlation between the ion anisotropies at the two wavelengths for individual ions.

Fig. 7.11 shows the local PDG contributions from signal and pump PHB predicted by our model, plotted versus the signal power P_s for fully polarized pump and laser signals. The pump power and gain medium parameters are the same as for the simulations in Figs. 7.9 and 7.10. We see that both the signal and the pump induced PDG have maxima near the saturation signal power $P_{sat} = 15.5$ dBm. The signal induced PDG scales proportionally with the signal DOP, which is essentially constant throughout the cavity, and equal to the output DOP $D_p = (P_x - P_y)/(P_x + P_y)$. Similarly, the pump induced PDG is proportional to the pump DOP D_{pp}. It is found from Figs. 7.9 and 7.10 that D_p increases with about 0.5 in the dual polarization regimes when D_{pp} is reduced by 2 by changing from x-polarized to y-polarized pump. To maintain lasing in both polarizations, any difference in round-trip gain contributed from the gain medium must be maintained when D_{pp} and D_p changes. This condition is satisfied when the sum of the integrals over z of the signal and pump induced PDG contributions, weighted by the intensity distribution $P_s(z)$, is unchanged. The calculated laser power distribution for DFBa, averaged over one standing wave period, $\overline{P_s}(z)$, is illustrated with z referenced to the right-hand axis in Fig. 7.11. (The power distribution for DFBb has also been calculated, and was

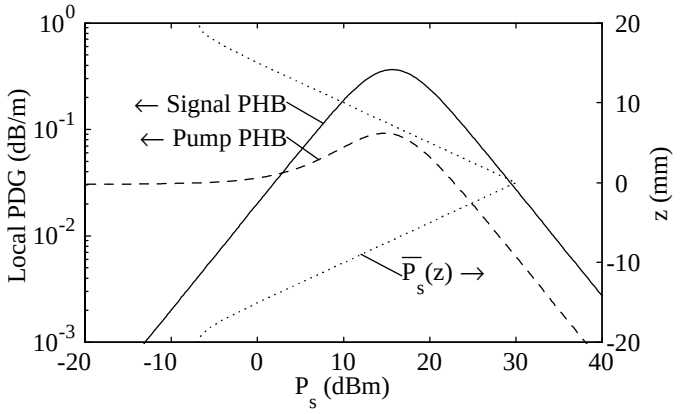

Figure 7.11. Contributions to the local signal PDG originating from signal PHB (solid line) and pump PHB (dashed lines), plotted against signal power P_s for a pump power of $P_p = 83$ mW. The pump and signal are assumed to be fully polarized. The calculated laser power distribution $\overline{P_s}(z)$ in DFBa is also shown. Parameters: $D_{pp} = -D_p = 1$, $\eta = 0.12$, $\eta_p = 0.021$, $[a_s, a_p, g_s, g_p] = [11.7, 8.9, 5.9, 3.0]$ dB/m, $P_{sp} = 4.1$ mW/m, $\xi = 39$ %, $\zeta = 25$.

found to be similar in peak magnitude and exponential decay rate to that of DFBa.) We see from the figure that most of the integrated PDG contributions will originate from the region -7 mm $< z < 7$ mm. In this region $\overline{P_s}(z) \gtrsim P_{sat}$, and the pump PHB is suppressed relative to the signal PHB by a factor that is close to $\eta_p/\eta \approx 0.18$.

In lasers with mirror transmissivities $T_1$and T_2 that exceeds the mirror transmissivities the investigated lasers by more than 15 dB, the peak cavity intensity will be more than 15 dB lower for similar output powers. We see from Fig. 7.11 that the ratio between the pump and the signal PHB magnitudes is higher in this case. Therefore, the PMC is expected to be more sensitive to the pump DOP in high mirror transmissivity lasers.

7.6 Conclusion

We have investigated how the polarization mode competition, polarization beat frequency, and individual modal frequencies in fiber DFB lasers depend on localized transverse force induced birefringence, back reflections and pump polarization. Theoretical results obtained from a comprehensive simulation model show good agreement with the measurements. Since the model parameters are obtained from independent informations that were extracted from a variety of measurements, the validity of the model is believed to be well verified.

The decrease in PHB at high saturating powers predicted by the model (c.f. Fig. 7.11) could not be checked very well by the presented measurements, however, since the peak intensity in laser cavities have been similar in all the measurements. The theory describing PHB effects at lower saturating powers have been verified from experiments in earlier publications [15]. The signal PHB parameter $\eta = 0.12$ estimated from the present measurements is twice as high as the value estimated in [8b] from measurements reported in [15] on erbium doped fiber amplifiers. Our higher value for η may be due to different compositions for the laser and the EDFA fibers, or it may be related to the grating fabrication process, including D_2-loading and UV exposure.

We have shown how the gain model presented in [8] can be extended to cover effects of PHB at the pump wavelength. The estimated pump PHB parameter $\eta_p = 0.021$ is significantly smaller than η, allowing for stable dual polarization operation independent on pump polarization. Fluctuations in the pump polarization are found to cause variations in the laser output degree of polarization D_p by ± 0.25.

We have shown that the transverse force sensitivity of a dual polarization fiber DFB laser sensor can be increased significantly compared to the sensitivity achieved by pressing uniformly along the whole length of the laser by concentrating the force to within a distance shorter than $1/2\kappa$ from the grating phase-shift position. Eq. (7.1) predicts that the sensitivity can be enhanced by a factor of κL (typically 10) in this way. In our experiment we measured a transverse force sensitivity of 1.6 GHz/N, with good linearity over the full dynamic range of ~ 1.5 N. The dynamic range is limited by fading of one of the laser modes as the polarization dependence of the grating phase-shift increases.

We have found that possible UV-induced loss gratings, either formed by lifetime-quenched ions or by unbleachable losses, will influence how the PMC depends on a polarization dependent grating phase-shift. The effects on the PMC of such a loss grating is similar to the effects of a polarization independent bias in the grating phase-shift. There exist clear indications, both from investigations of the laser slope efficiencies and relaxation oscillation stability margins, that UV-induced lifetime-quenching is present in the investigated lasers [11]. It is not, however, verified to which degree the quenching has a grating component.

The tolerable external back reflection level to maintain dual polarization operation is found to be -24 dB for the symmetric DFBa. This limit is expected to increase with increasing η. It is not expected to depend much on the grating strength κL, provided that κL is well above its threshold value for lasing [8b]. For the asymmetric DFBb, the tolerable back reflection level was -32 dB at the high output port and -4.4 dB (simulated) at the low output port.

The beat frequency noise has been measured for one of the lasers to decrease from 120 to 2.1 Hz/$\sqrt{\text{Hz}}$ between 20 Hz and 40 kHz. For a force sensor this corresponds to a noise equivalent force ranging from 75 and 1.3 nN/$\sqrt{\text{Hz}}$. If the DC temperature sensitivity reported in [3] is assumed to be valid up to 40 kHz, a noise equivalent temperature fluctuation between 75 and 1.3 μK/$\sqrt{\text{Hz}}$ is found. The sensitivity to external temperatures is, however, expected to decrease above 100 Hz due to the limited radial thermal conductivity of the fiber. The source of the observed noise floor has not been identified. Beat frequency noise contributions from Schawlow-Townes noise, shot-noise, and fundamental temperature noise are all estimated to be below 0.1 Hz/$\sqrt{\text{Hz}}$. The results in Fig. 7.7 (c) indicate that external back reflections with random phase fluctuations may be a significant noise source. Such phase fluctuations could either originate from optical path length fluctuations in the external cavity, or from common-mode laser frequency noise.

7.7 Acknowledgment

The first author acknowledges K. Bløtekjær, S. W. Løvseth and J. T. Kringlebotn for valuable help with reading through and commenting earlier versions of this manuscript. This work was sponsored by Optoplan AS, Norwegian Research Council and British Council. The ORC is an EPSRC (UK) funded interdisciplinary Research Centre.

Appendix:

7.A Modifications to the Gain and PHB Models

The gain model used for the simulations in this paper is based on the model derived in [8]. The gain coupling matrix $\mathbf{G}$ has been slightly modified, taking the form:

$$\mathbf{G} = \begin{bmatrix} g_x & 0 & g_{gr,x} & 0 \\ 0 & g_y & 0 & g_{gr,y} \\ -g^*_{gr,x} & 0 & -g_x & 0 \\ 0 & -g^*_{gr,y} & 0 & -g_y \end{bmatrix} \tag{7.3}$$

with

$$\begin{aligned} g_x &= g - (1 - D_p)\,(\Delta g_s + \Delta g_p) \\ g_y &= g + (1 + D_p)\,(\Delta g_s + \Delta g_p) \\ g_{gr,x} &= g_{gr} - (1 - D_p)\,(\Delta g_{gr,s} + \Delta g_{gr,p}) \\ g_{gr,y} &= g_{gr} + (1 + D_p)\,(\Delta g_{gr,s} + \Delta g_{gr,p})\,. \end{aligned} \tag{7.4}$$

Here, g_q and $g_{gr,q}$ are the gain and gain grating coefficients, respectively, in the $q = x, y$ polarization propagation modes. $g_x - g_y = \Delta g_s + \Delta g_p$ and $g_{gr,x} - g_{gr,y} = \Delta g_{gr,s} + \Delta g_{gr,p}$ are the polarization dependencies of the gain and gain gratings due to polarization hole burning (PHB) at the signal (subscript s) and pump (subscript p) wavelengths. D_p is the linear degree of polarization (DOP) of the lasing signal, defined by [8a] (8). The main modification to the form of $\mathbf{G}$ compared to [8] is that the pump polarization dependent parameters Δg_p and $\Delta g_{gr,p}$ have been included. A further modification is that the polarization dependent gain (PDG) components in (7.4) are divided between the x and y modes (through the factors $(1 \pm D_p)$) in a way such that the energy conservation budget, taking into account pump absorption, signal gain, and spontaneous emission, is satisfied independent on D_p.

Lifetime quenching of a fraction ξ of the ions by a factor ζ is modeled by assuming two gain media numbered $k = 1, 2$ with ion concentrations $n_k = w_k N$. $w_1 = (1-\xi)$, $w_2 = \xi$, and N is the total ion concentration. The local saturated amplitude gain $g_{loc,k}$ for medium k, may be expressed according to [8a] as:

$$\begin{aligned} g_{loc,k}(\phi) &= n_k N^{-1} g_{unsat,k} \left(1 + P_s(\phi)/P_{sat,k}\right)^{-1} \\ g_{unsat,k} &= w_k \left(a_p r_{wl} P_p / P_{sat,k} - a_s\right) \\ P_{sat,k} &= \left[\left(g_p + a_p\right) r_{wl} P_p + P_{sp,k}/2\right] \left(g_s + a_s\right)^{-1} \end{aligned} \tag{7.5}$$

Here, $g_{unsat,k}$ is the mean unsaturated gain and P_{sat} is the saturation power. P_p is the pump power, and $P_s(\phi) = \sum_{q=x,y} |\vec{R}_q + \vec{S}_q \exp(i\phi)|^2$ is the total saturating power where $\vec{R}_q$ and $\vec{S}_q$ are the right and left propagating fields of the $q = x, y$ lasing modes. P_{sp}, g_s, g_p, a_s, and a_p are the gain medium parameters without quenching, as defined in Sec. 7.2, $P_{sp,1} = (1-\xi)P_{sp}$, and $P_{sp,2} = \zeta\xi P_{sp}$. $r_{wl} = 1480/1549$ is the ratio of the pump wavelength to the signal wavelength. The gain g_k and gain grating $g_{gr,k}$ coefficients of each gain medium may be expressed as

$$g_k = \frac{g_{unsat,k}}{R}; \quad g_{gr,k} = g_k \frac{R - a}{b^*},$$

with

$$a = 1 + \frac{P_t}{P_{sat,k}}, \quad b = \frac{2P_c}{P_{sat,k}}, \quad R = \sqrt{a^2 - |b|^2}, \tag{7.6}$$

$$P_t = \sum_{q=x,y} \left|\vec{R}_q\right|^2 + \left|\vec{S}_q\right|^2, \quad P_c = \sum_{q=x,y} \vec{S}_q^{+} \vec{R}_q. \tag{7.7}$$

$\vec{S}_q^{+}$ is the conjugate transpose of $\vec{S}_q$.

An expression for the local signal induced polarization dependence of the gain due to the ion cross section anisotropies was deduced in [8b] (1):

$$\Delta g_{loc,k}(\phi) = \frac{D_p \eta g_{unsat,k}\, n_k(\phi)}{N} \times \frac{P_s(\phi)/P_{sat,k}}{\left(1 + P_s(\phi)/P_{sat,k}\right)^2}. \tag{7.8}$$

Here, η is the PHB parameter at the signal wavelength. (7.8) may be expressed as $\Delta g_{loc,k} = f_k(\phi)$ where

$$f_k(\phi) = v\frac{c + \mathrm{Re}\left\{be^{i\phi}\right\}}{\left(a + \mathrm{Re}\left\{be^{i\phi}\right\}\right)^2}, \tag{7.9}$$

$v = w_k \eta D_p\, g_{unsat,k}$, $c = a - 1$, and a and b are defined by (7.6). The zeroth and first order Fourier components of $f_k(\phi)$ are:

$$F_{0,k} = \frac{1}{2\pi}\int_0^{2\pi} f(\phi)\, d\phi = v\frac{aB^2c - B^4}{QB^2}, \tag{7.10}$$

$$F_{1,k} = \frac{1}{2\pi}\int_0^{2\pi} f(\phi)\, e^{-i\phi} d\phi = vb^*\frac{aB^2 - a^3 - B^2c + Q}{QB^2} \tag{7.11}$$

respectively, where

$$B = |b| \text{ and } Q = \left(a^2 - B^2\right)^{3/2}.$$

The signal induced polarization dependence of the gain and gain grating coefficients are found as $\Delta g_s = F_{0,1} + F_{0,2}$ and $\Delta g_{gr,s} = F_{1,1} + F_{1,2}$, respectively

The pump induced PDG may be modeled on basis of the same theory [8b] that was used to arrive at (7.8) by assuming the existence of ion cross-section anisotropy also at the pump wavelength. We first exchange the roles of the pump and the signal in (7.5) and (7.8) by exchanging $\Delta g_{loc,k}$, P_s, g_s, a_s, g_p, a_p, r_{wl}, $P_{sp,k}$, η, and D_p with $\Delta g_{loc,p,k}$, P_p, g_p, a_p, g_s, a_s, r_{wl}^{-1}, $P_{sp,k}/r_{wl}$, η_{p0}, and D_{pp} respectively, where, $\Delta g_{loc,p,k}$ is the polarization dependence of the (negative) gain at the pump wavelength. η_{p0} depends on the ion anisotropy at the pump wavelength in the same way as η depends on the ion anisotropy at the signal wavelength [8b]. $D_{pp} = (P_{px} - P_{py}) / (P_{px} + P_{py})$ is the linear DOP of the pump signal, where P_{px} and P_{py} are the x- and y-polarized components of P_p, respectively. The resulting PDG at the signal wavelength may be written $\Delta g_{loc,s,k} = r_1 r_0 \Delta g_{loc,p,k}$, where $r_0 = (g_s + a_s) / (g_p + a_p)$ is the conversion factor from pump to signal gain changes, and r_1 accounts for the possibility that the cross section anisotropies of individual ions at the two wavelengths may not be fully correlated. After some algebraic manipulation, the local PDG may be written on the form $\Delta g_{loc,s,k} = f_k(\phi)$ if the parameters a, b, c and v in (7.9)

are redefined as:

$$\begin{aligned} a &= 1 + (P_t + P_{sp,k}/2)\, P_0^{-1}, & b &= 2P_c P_0^{-1} \\ c &= \left(P_t + \frac{r_0 a_p\, P_{sp,k}/2}{r_0 a_p - a_s} \right) P_0^{-1}, & P_0 &= r_{wl} P_p r_0^{-1} \\ v &= -w_k \eta_p\, D_{pp}\, (r_0 a_p - a_s) & \eta_p &= r_1 \eta_{p0}. \end{aligned} \tag{7.12}$$

P_t and P_c are defined by (7.7). The pump induced portion of the polarization dependence of the gain and gain grating coefficients Δg_p and $\Delta g_{gr,p}$, respectively, may thus be calculated, after substituting (7.12) into (7.10, 7.11), as $\Delta g_p = F_{0,1} + F_{0,2}$ and $\Delta g_{gr,p} = F_{1,1} + F_{1,2}$.

References

[1] M. Ibsen, A. Fu, H. Geiger and R.I. Laming, "All-fibre 4 x 10 Gbit/s WDM link with DFB fibre laser transmitters and a single sinc-sampled fibre grating dispersion compensator", Electron. Lett., Vol. 35, pp. 982-983, 1999.

[2] J. T. Kringlebotn, W. H. Loh and R. I. Laming, "Polarimetric Er^{3+}-doped fiber distributed-feedback laser sensor for differential pressure and force measurements", Opt. Letters, Vol.21, pp.1869-71, 1996.

[3] O. Hadeler, E. Rønnekleiv, M. Ibsen and R. I. Laming, "Polarimetric fiber distributed feedback laser sensor for simultaneous strain and temperature measurements", Appl. Opt., Vol. 38, pp. 1953-1958, 1999.

[4] H. Storøy, B. Sahlgren and R. Stubbe, "Single polarization fibre DFB laser", El. Letters, Vol. 33, pp. 56-8, 1997.

[5] J. I. Philipsen, M. O. Berendt, P. Varming, V. C. Lauridsen, J. H. Povlsen, J. Hübner, M. Kristensen, B. Pálsdóttir, "Polarisation control of DFB fibre laser using UV-induced birefringent phase-shift", El. Letters, Vol. 34, pp. 678-9, 1998.

[6] M. Ibsen, E. Rønnekleiv, G. J. Cowle, M. O. Berendt, O. Hadeler, M. N. Zervas, and R. I. Laming, "Robust high-power (>20 mW) all-fiber DFB lasers with unidirectional and truly single polarization outputs" in *Proc. to Conference on Lasers and Electro-Optics (CLEO) 1999*, pp. 245-246, paper CWE4, Baltimore, USA, 1999.

[7] Z. E. Haratjunian, W. H. Loh, R. I. Laming and D. N. Payne, "Single polarization twisted distributed feedback fibre laser", El. Lett., Vol. 32, pp. 346-8, 1996.

[8] a) E. Rønnekleiv, M. N. Zervas and J. T. Kringlebotn, "Modeling of Polarization Mode Competition in Fiber DFB Lasers", IEEE J. Quantum Electron., Vol. 34, pp. 1559-69, 1998.
b) E. Rønnekleiv, M. N. Zervas and J. T. Kringlebotn, "Correction to "Modeling of Polarization Mode Competition in Fiber DFB Lasers"", IEEE J. Quantum Electron., Vol. 35, pp. 1097-1100, 1999.

[9] E. Rønnekleiv, M. Ibsen, M. N. Zervas, and R. I. Laming, "Characterization of fiber distributed-feedback lasers with an index perturbation method", Appl. Opt., Vol. 38, pp. 4558-4565, 1999.

[10] L. Dong, W. H. Loh, J. E. Caplen, J. D. Minelly and L. Reekie, "Efficient single-frequency fiber-lasers with novel photosensitive Er/Yb optical fibers", Opt. Lett., Vol. 22, pp. 694-6, 1997.

[11] E. Rønnekleiv and O. Hadeler, "Stability of an Er-Yb-doped fiber distributed-feedback laser with external reflections", Opt. Lett., Vol. 24, pp. 617-619, 1999.

[12] J. Hübner, T. Feuchter, C.V. Poulsen, and M. Kristensen, "Directly UV-written erbium doped waveguides", in *Photosensitivity and Quadratic Nonlinearity in Glass Waveguides: Fundamentals and Applications*, OSA Technical Digest Series, Vol. 22, 1995.

[13] J. I. Sakai, T. Kimura, "Birefringence and Polarization Characteristics of Single-Mode Optical Fibers under Elastic Deformations", IEEE J. of Q. El., Vol. QE-17, pp. 1041-51, 1981.

[14] R. B. Wagreich, W. A. Atia, H. Singh and J. S. Sirkis, "Effects of diametric load on fibre Bragg gratings fabricated in low birefringent fibre", El. Letters, Vol. 32, pp. 1223-4, 1996.

[15] P. Wysocki and V. Mazurkzyk, "Polarization Dependent Gain in Erbium-doped Fiber Amplifiers: Computer Model and Approximate Formulas", J. Lightwave Technol., Vol. 14, pp. 572-84, 1996.

[16] M. Sargent III, W. H. Swantner and J. D. Thomas, "Theory of a Distributed Feedback Laser", IEEE J. of Q. El., Vol. QE-16, pp. 465-72, 1980.

[17] W. S. Rabinovich and B. J. Feldman, "Spatial Hole Burning Effect in Distributed Feedback Lasers", IEEE J. of Q. El., Vol. 25, pp. 20-30, 1989.